



**Abstract**

We study the effects of pore fluid pressure ( $P_f$ ) on the pre-earthquake, near-fault stress state and 3D earthquake rupture dynamics through 6 scenarios utilizing a structural model based on the 2004  $M_w$  9.1 Sumatra-Andaman earthquake. As pre-earthquake  $P_f$  magnitude increases, effective normal stress and fault shear strength decrease. As a result, magnitude, slip, peak slip rate, stress drop and rupture velocity of the scenario earthquakes decrease. Comparison of results with observations of the 2004 earthquake support that pre-earthquake  $P_f$  averages near 97 % of lithostatic pressure, leading to pre-earthquake average shear and effective normal tractions of 4-5 MPa and 22 MPa. The megathrust in these scenarios is weak, in terms of low mean shear traction at static failure and low dynamic friction coefficient during rupture. Apparent co-seismic principal stress rotations and absolute post-seismic stresses in these scenarios are consistent with the variety of observed aftershock focal mechanisms. In all scenarios, the mean apparent stress rotations are larger above than below the megathrust. Scenarios with larger  $P_f$  magnitudes exhibit lower mean apparent principal stress rotations. We further evaluate pre-earthquake  $P_f$  depth distribution. If  $P_f$  follows a sublithostatic gradient, pre-earthquake effective normal stress increases with depth. If  $P_f$  follows the lithostatic gradient exactly, then this normal stress is constant, shifting peak slip and peak slip rate up-dip. This renders constraints on near-trench strength and constitutive behavior crucial for mitigating hazard. These scenarios provide opportunity for future calibration with site-specific measurements to constrain dynamically plausible megathrust strength and  $P_f$  gradients.

**Plain Language Summary**

Large volumes of fluid can lead to high pressures that weaken rocks in fault zones and influence earthquake rupture. While fluids are critical to understanding behavior at subduction zones, where the largest earthquakes in the world occur and where tsunami generation increases hazard, measuring fluid and fluid pressure directly across an entire megathrust currently is not possible. Here, we use supercomputers to model the devastating 2004 Mw 9.1 Sumatra-Andaman earthquake in 3D in order to isolate the role of fluid pressure on earthquake behavior. By first building a reliable base model and then varying fluid pressure to generate 6 earthquake scenarios, we find that fluid pressure is likely very high, and also that the way that fluid pressure varies with depth can greatly influence the earthquake and associated hazard. Fluid pressure controls location of the largest and fastest fault slip along the megathrust, and the possibility for a devastating tsunami.

**1 Introduction**

High pore fluid pressures in subduction zones are expected due to the low rates of diffusion and the numerous geologic processes that produce fluids (Saffer & Tobin, 2011). Indications of overpressure, i.e. when pore fluid pressure ( $P_f$ ) is above the hydrostatic pressure gradient, include observations of extensional veining (Rowe et al., 2009) and high seismic reflectivity (e.g., Calahorrano et al., 2008). These observations indicate  $P_f$  at 75 % of the lithostatic load at Nankai (Tobin & Saffer, 2009), while shallow boreholes indicate  $P_f$  at up to 97 % of the lithostatic pressure (Saffer & Tobin, 2011). At Cascadia, high ratios of P-wave to S-wave speed ( $V_p/V_s$ ) observed from receiver functions are inconsistent with lithology, but can be explained by near-lithostatic  $P_f$  (Audet et al., 2009).

$P_f$  differences are thought to explain spatial and temporal variations in slip behavior observed in subduction zones (e.g., Saffer & Tobin, 2011; Audet & Schwartz, 2013; Gao & Wang, 2017; Saffer, 2017). At the base of the seismogenic zone, high  $P_f$  is linked to low effective normal stress conditions and slow earthquake slip behavior (Rice, 2006; Liu & Rice, 2007; Shelly et al., 2007; Bürgmann, 2018). Slow slip earthquakes observed

66 deep along the Cascadia subduction zone are attributed to hydrofracturing of the bar-  
 67 rier trapping fluids in the down-going plate, allowing fluids to circulate (Audet et al., 2009).  
 68 Fluid circulation under high pressure also may be responsible for low frequency tremor  
 69 and rapid tremor migration (Beeler et al., 2013; Cruz-Atienza et al., 2018). Tremor in  
 70 the Japan trench is co-located with regions of high  $P_f$  (Shelly et al., 2006). Deep tremor  
 71 at the Livingstone Fault in New Zealand appears co-located with regions of high  $P_f$  caused  
 72 by serpentinite reactions near the slab-mantle interface (Tarling et al., 2019). Both tremor  
 73 and slow slip have been linked to the very small changes in pressure from tidal stress,  
 74 suggesting weak faults and high  $P_f$  (Houston, 2015; Tonegawa et al., 2021).

75 In seismogenic regions of subduction zones, lower  $P_f$  conditions have been proposed  
 76 as a mechanism for locking (Saffer & Tobin, 2011). Heise et al. (2017) co-locate a geodetically-  
 77 identified locked region with a patch of high electrical resistivity attributed to lack of fluid  
 78 or low  $P_f$  on the Hikurangi subduction interface, while shallow creep occurs in a region  
 79 of conductivity that can be explained by high fluid production or high  $P_f$  (Heise et al.,  
 80 2013). However, heat flow studies (Gao & Wang, 2014) and force-balance inversions (Lamb,  
 81 2006) find shear to normal stress ratios that indicate high  $P_f$  near the megathrust. Lamb  
 82 (2006) finds evidence for  $P_f$  at 95 % of the lithostatic pressure at 7 of 9 subduction zones,  
 83 including Sumatra. Two exceptions to this are Northern Chile and Tonga, with  $P_f$  at  
 84 81 % of the lithostatic pressure.

85 Temporal variation in  $P_f$  is central to the fault-valve model of Sibson (1992, 1994),  
 86 which attributes earthquakes to both tectonic loading (shear stress building up until an  
 87 earthquake occurs) and fluid-pressure cycling ( $P_f$  building up and effective normal stress  
 88 falling over time until an earthquake occurs). Petrini et al. (2020) show that fluid pres-  
 89 sure variations in time can control subduction zone seismic cycling. Analyses of bore-  
 90 hole fluids suggest cycles of 10,000-100,000 years (Saffer & Tobin, 2011), which may cor-  
 91 relate with fault formation, while shorter period variations correlate with slow slip events  
 92 in Costa Rica. In addition, observed increases in  $V_p/V_s$  following the 1995 M 8 Antofa-  
 93 gasta earthquake (Husen & Kissling, 2002) suggest the rapid movement of fluid during  
 94 or directly after megathrust earthquakes. Eberhart-Phillips et al. (1989) note that such  
 95 changes can occur only when  $P_f$  is near-lithostatic.

96 This variety of observations and inferences about  $P_f$  in subduction zones is reflected  
 97 in the variety of ways that  $P_f$  is considered in faulting and earthquake models. Quasistatic  
 98 models of fault slip may not incorporate  $P_f$  explicitly, but set stress gradients that pro-  
 99 duce reasonable fault slip distributions (e.g., Madden & Pollard, 2012; Madden et al.,  
 100 2013). Models of earthquake sequences and rupture dynamics commonly prescribe nor-  
 101 mal stress following effective stress theory as  $\sigma_n - P_f$ , where  $\sigma_n$  is the normal stress (Hubbert  
 102 & Rubey, 1959; Brace & Kohlstedt, 1980).  $P_f$  typically increases with depth and is cho-  
 103 sen ad-hoc to help reconcile realistic earthquake characteristics with friction and fault  
 104 shear strength (Liu & Rice, 2005; Kozdon & Dunham, 2013; Wollherr et al., 2019; Ul-  
 105 rich, Gabriel, et al., 2019). Uphoff et al. (2017) and Ulrich et al. (2022) incorporate near-  
 106 lithostatic  $P_f$  following depth-dependent gradients into large-scale, three-dimensional dy-  
 107 namic rupture models. Others initialize dynamic rupture models with conditions, includ-  
 108 ing initial  $P_f$ , from geodynamic and seismic cycling modeling that captures long term  
 109 subduction zone deformation and fluid flow (I. Zelst et al., 2019; Wirp et al., 2021; Mad-  
 110 den et al., 2021).

111 Rice (1992) shows that fluid at elevated pressures within a fault zone may follow  
 112 the same gradient with depth as the lithostatic stress, causing constant effective normal  
 113 stress with depth. Data from crustal sedimentary rocks support this theory (Suppe, 2014).  
 114 This condition is assumed in some dynamic rupture models (e.g., Ramos & Huang, 2019;  
 115 Ramos et al., 2021), but not others (e.g., Kozdon & Dunham, 2013; Lotto et al., 2019;  
 116 Ulrich, Vater, et al., 2019; Ulrich et al., 2022). Other models consider the coupled, dy-  
 117 namic effects of fluids, such as dilatancy (e.g., Segall & Rice, 1995; Aochi et al., 2014)  
 118 and thermal pressurization (e.g., Rice, 2006; Schmitt et al., 2011; Segall & Bradley, 2012;

Garagash, 2012). Recent two-dimensional (2-D) antiplane earthquake sequence modeling by Zhu et al. (2020) couples earthquake and pore fluid dynamics by incorporating fluid migration and periodic  $P_f$  variations over earthquake cycles. These models produce fluid-driven aseismic slip at the base of the seismic zone, large earthquakes, and earthquake swarms. 2-D seismo-hydro-mechanical modeling of subduction zone earthquake cycling shows high  $P_f$  moving progressively up-dip due to compaction inside an evolving fault, eventually leading to a seismic event (Petrini et al., 2020).

$P_f$  prior to an earthquake can be constrained by these observations and inferences with simultaneous consideration of the normal stress and static frictional strength of a megathrust, but it has not been measured directly and little data is available, particularly deep along subduction zones. Few studies integrate knowledge about megathrust mechanics with megathrust earthquake rupture dynamics to study  $P_f$  at the time of rupture. Specifically, three-dimensional (3-D) dynamic simulations at the megathrust scale that take realistic slab geometries into account remain challenging. To supplement this gap, we explore the dynamic effects of different hypotheses about  $P_f$  magnitude and gradient in megathrust systems using a 3-D dynamic earthquake rupture and seismic wave propagation model that matches near- and far-field seismic, geodetic, geologic, and tsunami observations of the 2004 Sumatra-Andaman earthquake and Indian Ocean tsunami (Uphoff et al., 2017; Ulrich et al., 2022).

Our focus is to highlight the effects of pre-earthquake  $P_f$  conditions on earthquake behavior within a structurally complex megathrust system. We analyze how various hypotheses on  $P_f$  magnitude and depth gradient affect the pre-earthquake stress state near a megathrust, the subsequent earthquake rupture characteristics, and the postseismic stress field. Specifically, we generate 6 scenario earthquakes with  $P_f$  magnitudes at 31 %, 62 %, 93 % and 97 % of the lithostatic pressure and under two different depth gradients that cause either increasing or constant normal stress near the megathrust. We compare results against observations of the 2004 earthquake as well as general observational inferences about subduction zone earthquakes.

We note that the range of pre-earthquake conditions captured by our 6 scenarios may reflect the variety of conditions present along a single megathrust at the same time, due to spatial variations in  $P_f$  magnitude and/or gradient. In addition, hydromechanical processes likely vary in space and time as a consequence of rock deformation processes that modulate the permeability of both fault and host rocks, in turn affecting fluid diffusion. Coupling these processes during the full seismic cycle to determine realistic fluid conditions at the start of earthquake rupture is a clear future step. However, modeling these processes in 3-D is beyond the state of the art, despite the recent progress of 2-D numerical models reviewed above. Our results provide key advances regarding the influence of  $P_f$  on earthquake behavior and provide opportunity for future calibration with site-specific friction and pore-fluid measurements to constrain dynamically plausible megathrust strength and  $P_f$  gradients.

## 2 Modeling methods

### 2.1 Computational model

The earthquake models are performed with SeisSol ([www.seissol.org](http://www.seissol.org)), a software package that solves for dynamic fault rupture and seismic wave propagation with high-order accuracy in space and time. SeisSol solves the seismic wave equation in velocity-stress formulation using an Arbitrary high-order DERivate Discontinuous Galerkin (ADER-DG) scheme (Dumbser & Käser, 2006). Computational optimizations target supercomputers with many-core CPUs (Breuer et al., 2014; Heinecke et al., 2014; Rettenberger et al., 2016; Krenz et al., 2021). SeisSol uses local time stepping, which increases runtime efficiency by decreasing dependence of the time-step on the element with the small-

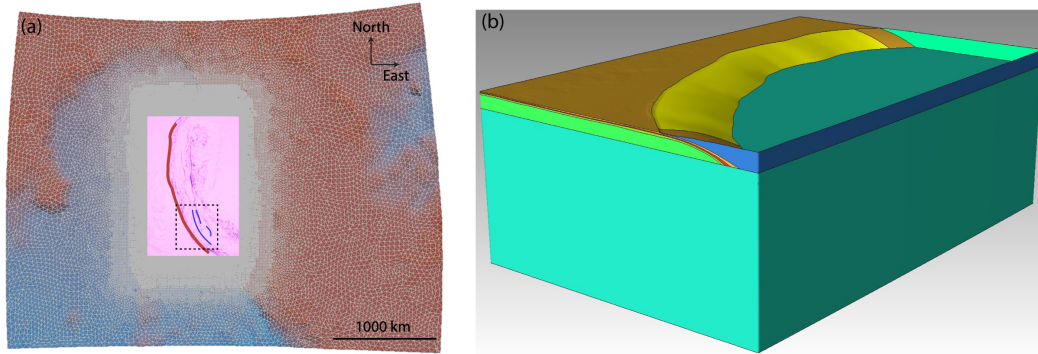


**Figure 1.** (a) Surface of model demonstrating adaptive meshing in grey. Mesh resolution is finer within the pink box to resolve the topography at the surface and the megathrust and splay faults at depth. Dark red is land and blue is water. Red line is megathrust trace. Dashed black lines highlight the splay fault region and blue lines are the traces of the three splay faults included in model. Figure adapted from Uphoff et al. (2017). Mesh details differ from Uphoff et al. (2017) and are included in Appendix A. (b) Zoom to oblique view of the pink region in (a). Yellow surface is the megathrust, which intersects the seafloor to left and reaches 50 km depth to right. Splays faults not shown, but extend from megathrust to surface. A lower-velocity subduction channel surrounds the megathrust (Table 1). Layers of oceanic crust are horizontal away from the megathrust and curve below it; these are meshed. The continental crust above and right of megathrust is not shown, except by blue border to right. Properties are assigned to layers of continental crust by depth; these layers are not meshed.

169 est radius (Breuer et al., 2016; Uphoff et al., 2017; Wolf et al., 2020). Following the SCEC/USGS  
 170 Dynamic Rupture Code Verification exercises (Harris et al., 2009, 2018), SeisSol has been  
 171 validated against several community benchmarks (De La Puente et al., 2009; Pelties et  
 172 al., 2012, 2014; Wollherr et al., 2018).

## 173 2.2 Structural model

174 The structural model and computational mesh are shown in Figure 1. Use of an  
 175 unstructured tetrahedral mesh allows for a realistic representation of the non-planar slab  
 176 interface, splay faults, curved oceanic crust and high-resolution bathymetry. The megathrust  
 177 geometry follows Slab1.0 (Hayes et al., 2012). The splay faults, one longer backthrust and  
 178 two shorter forethrusts, are interpreted from aftershocks (Waldhauser et al., 2012),  
 179 seafloor observations (Sibuet et al., 2007; Chauhan et al., 2009; Singh et al., 2008) and  
 180 tsunami modeling (DeDontney & Rice, 2011). The mesh for this model has elements with  
 181 edge lengths of 1 km along the faults, 4 km at the surface, and 100 km in the volume  
 182 far from the fault; mesh resolution varies gradually between these conditions. We ensure  
 183 that the element size along the megathrust and splay faults is sufficient to capture the  
 184 cohesive zone following the analysis in Wollherr et al. (2018) and detailed in Appendix  
 185 A.

186 The regional rock properties are adapted from Laske et al. (2013) and include four  
 187 layers of oceanic crust and four layers of continental crust with the properties outlined  
 188 in Table 1. As shown in Figure 1, the layers of oceanic crust are horizontal away from  
 189 the megathrust and curve downward under the megathrust. The continental crust layers  
 190 are flat everywhere. We assume a linear elastic constitutive law.

**Table 1.** Material properties

max depth (km)	$V_p$ (m/s)	$V_s$ (m/s)	$\rho$ ( $kg/m^3$ )
Continental crust			
6	6000	3500	2720
12	6600	3800	2860
23	7100	3900	3050
500	8000	4450	3300
Oceanic crust <sup>a</sup>			
6	6000	3500	2720 <sup>b</sup>
8	6600	3800	2860
12	7100	3900	3050
30	8000	4450	3300

<sup>a</sup>Max depths are for horizontal layers, away from megathrust.

<sup>b</sup>This layer surrounds the megathrust.

### 191 3 Model set-up and fault mechanics

192 We present six scenarios that all utilize the same structural model based on the 2004  
 193  $M_w$  9.1 Sumatra-Andaman earthquake following Uphoff et al. (2017). The scenarios vary  
 194 in pre-earthquake pore-fluid pressure ( $P_f$ ) magnitude and depth gradient, and thus vary  
 195 in pre-earthquake effective normal stress near the megathrust. In order to isolate the in-  
 196 fluence of  $P_f$  in these scenarios, we choose to scale the megathrust shear traction with  
 197 the effective normal traction and keep the static and dynamic friction coefficients con-  
 198 stant across all scenarios. We step through how these initial conditions are assigned for  
 199 each scenario in the next subsection, then present the dynamic rupture process and model  
 200 conditions in the following subsection.

#### 201 3.1 Fluid pressure, the regional stress field and fault tractions

202 We assume a laterally homogeneous regional stress tensor. Its orientation is from  
 203 an inversion of focal mechanisms near the hypocenter of the 2004 Sumatra-Andaman earth-  
 204 quake by Karagianni et al. (2015) (region 7.1.22). Taking a compression negative sign  
 205 convention, the maximum compressive stress ( $\sigma_3$ ) has an azimuth of  $225^\circ$  and plunges  
 206  $7^\circ$ . The intermediate principal stress ( $\sigma_2$ ) has an azimuth of  $315^\circ$  and plunges  $7^\circ$ . The  
 207 least compressive stress ( $\sigma_1$ ) has an azimuth of  $90^\circ$  and plunges  $80^\circ$ . In all scenarios, the  
 208 absolute stresses are proportional to the lithostatic stress ( $\sigma_v = \rho g z$ , where  $\rho$  is the den-  
 209 sity of rock,  $g$  is gravitational acceleration and  $z$  is depth) as  $\sigma_1 = 0.98\sigma_v$ ,  $\sigma_2 = 1.5\sigma_v$ ,  
 210 and  $\sigma_3 = 2\sigma_v$ . Below 23 km depth, we taper the differential stress to zero at 50 km depth  
 211 to approximate the transition from brittle to ductile deformation.

212 We present six scenarios with different  $P_f$  magnitudes and depth gradients applied  
 213 to this absolute stress state (Table 2). Following the effective stress principle (Hubbert  
 214 & Rubey, 1959; Brace & Kohlstedt, 1980), the effective principal stresses ( $\sigma'_3 < \sigma'_2 <$   
 215  $\sigma'_1$ ) for each scenario are determined relative to the effective lithostatic stress,  $\sigma'_v = \sigma_v -$   
 216  $P_f$ . In Scenarios 1 to 4,  $P_f$  is applied as a percentage of  $\sigma_v$ , so we refer to this as a sub-  
 217 lithostatic  $P_f$  gradient.  $P_f$  is hydrostatic in Scenario 1 at 31% of  $\sigma_v$  and moderate in  
 218 Scenario 2 at 62% of  $\sigma_v$ . High and very high  $P_f$  in scenarios 3 and 4 are set to 93% and  
 219 97% of  $\sigma_v$ , respectively. The sublithostatic  $P_f$  gradient, the absolute principal stresses  
 220 and the effective principal stresses are shown for Scenario 4 in Figure 2a-c.

221 However, Rice (1992) shows that fluid at elevated pressures within a fault zone may  
 222 follow the same gradient with depth as  $\sigma_v$ , which causes a constant effective normal stress  
 223 with depth. We follow this assumption in scenarios 5 and 6, where high and very high  
 224  $P_f$  follow the gradient in  $\sigma_v$ , but are offset by constant values ( $K$ ) of 42 MPa in Scenario  
 225 5 and 20 MPa in Scenario 6:

$$P_f = \sigma_v - K \quad (1)$$

226 We refer to this as a lithostatic  $P_f$  gradient and it is applied below 5 km depth. To re-  
 227 semble borehole stress and fluid-pressure measurements in continental margins (e.g., Suppe,  
 228 2014), we apply a lithostatic gradient above 5 km in both scenarios. On average over the  
 229 rupture area,  $P_f$  in scenarios 5 and 6 is 93% and 97% of  $\sigma_v$ , respectively, mirroring val-  
 230 ues in scenarios 3 and 4. The lithostatic  $P_f$  gradient, the absolute principal stresses and  
 231 the effective principal stresses are shown for Scenario 6 in Figure 2d-f.

232 In all scenarios, stresses and  $P_f$  vary only with depth and do not vary with hor-  
 233 izontal location. As  $P_f$  increases in these scenarios, the magnitudes of  $\sigma'_v$ ,  $\sigma'_3$ ,  $\sigma'_2$  and  $\sigma'_1$   
 234 all decrease. In addition, the magnitudes of the effective mean stress and the effective  
 235 deviatoric stress decrease, so the effective normal stresses and the shear stresses decrease  
 236 as well. Figure 3a shows the relatively low stress magnitudes present at all orientations  
 237 when a very high  $P_f$  magnitude is applied in Scenario 4, while also demonstrating how  
 238 these stress magnitudes increase with depth in Scenarios 1-4. Figure 3b shows the rel-  
 239 atively low stress magnitudes present at all orientations when a very high  $P_f$  magnitude  
 240 is applied in Scenario 6, while also demonstrating how these stress magnitudes are con-  
 241 stant with depth in Scenarios 5 and 6.

242 The initial shear and effective normal tractions,  $\tau_s$  and  $\tau'_n$ , are determined by pro-  
 243 jecting the local effective stress tensors onto the non-planar megathrust and splay faults.  
 244 As for the shear and effective normal stresses, both  $\tau_s$  and  $\tau'_n$  decrease overall as  $P_f$  in-  
 245 creases from scenario to scenario. In Scenarios 1 to 4,  $\tau_s$  and  $\tau'_n$  increase with depth, while  
 246 in scenarios 5 and 6, both are relatively constant with depth. The pre-earthquake trac-  
 247 tions are shown for each scenario in Figure 4 and mean values are summarized in Ta-  
 248 ble 2. Setting the effective stress magnitudes relative to  $\sigma'_v$  as we do maintains the same  
 249  $\tau_s/\tau'_n$  distribution on the megathrust across all scenarios (Figure B1), which isolates the  
 250 influence of  $P_f$  on earthquake behavior, as desired in this study.

251 While the on-fault tractions mirror the near-fault stresses in many ways, our 3-D,  
 252 geometrically complex fault structure comprised of a non-planar megathrust and splay  
 253 faults modulates the fault traction distributions. As a result, they depart in certain lo-  
 254 cations from the linear stress gradients and feature additional spatial variations and het-  
 255 erogeneity, as both  $\tau_s$  and  $\tau'_n$  vary with fault geometry in all scenarios. Figure B1 illus-  
 256 trates how this distribution varies due to the non-planar megathrust geometry. In sce-  
 257 narios 5 and 6, where the  $P_f$  gradient is lithostatic and  $\tau_s$  and  $\tau'_n$  are relatively constant  
 258 with depth, the variation due to the megathrust geometry is  $\approx 5$  MPa.

### 259 3.2 Failure and spontaneous propagation

260 In all scenarios, dynamic earthquake rupture starts by forced nucleation in the south-  
 261 eastern corner of the megathrust at 30 km depth. Failure occurs when  $\tau_s$  exceeds the  
 262 static fault strength,  $T_{fs}$ , which is determined from the on-fault frictional cohesion,  $c$ ,  
 263 and the product of the coefficient of static friction,  $\mu_s$ , and  $\tau'_n$  as (compression is neg-  
 264 ative):

$$T_{fs} = c - \mu_s \tau'_n \quad (2)$$

265  $c$  is the frictional strength of a fault in the absence of  $\tau'_n$ . In-situ,  $c$  depends on local min-  
 266 eralogy and lithology, but here  $c$  is used as a standard proxy for near-surface behavior  
 267 that we do not model explicitly, mainly the constitutive behavior of shallow sediments  
 268 in the near-trench region (e.g., Kaneko et al., 2008; Harris et al., 2018). We set  $c = 0.4$  MPa

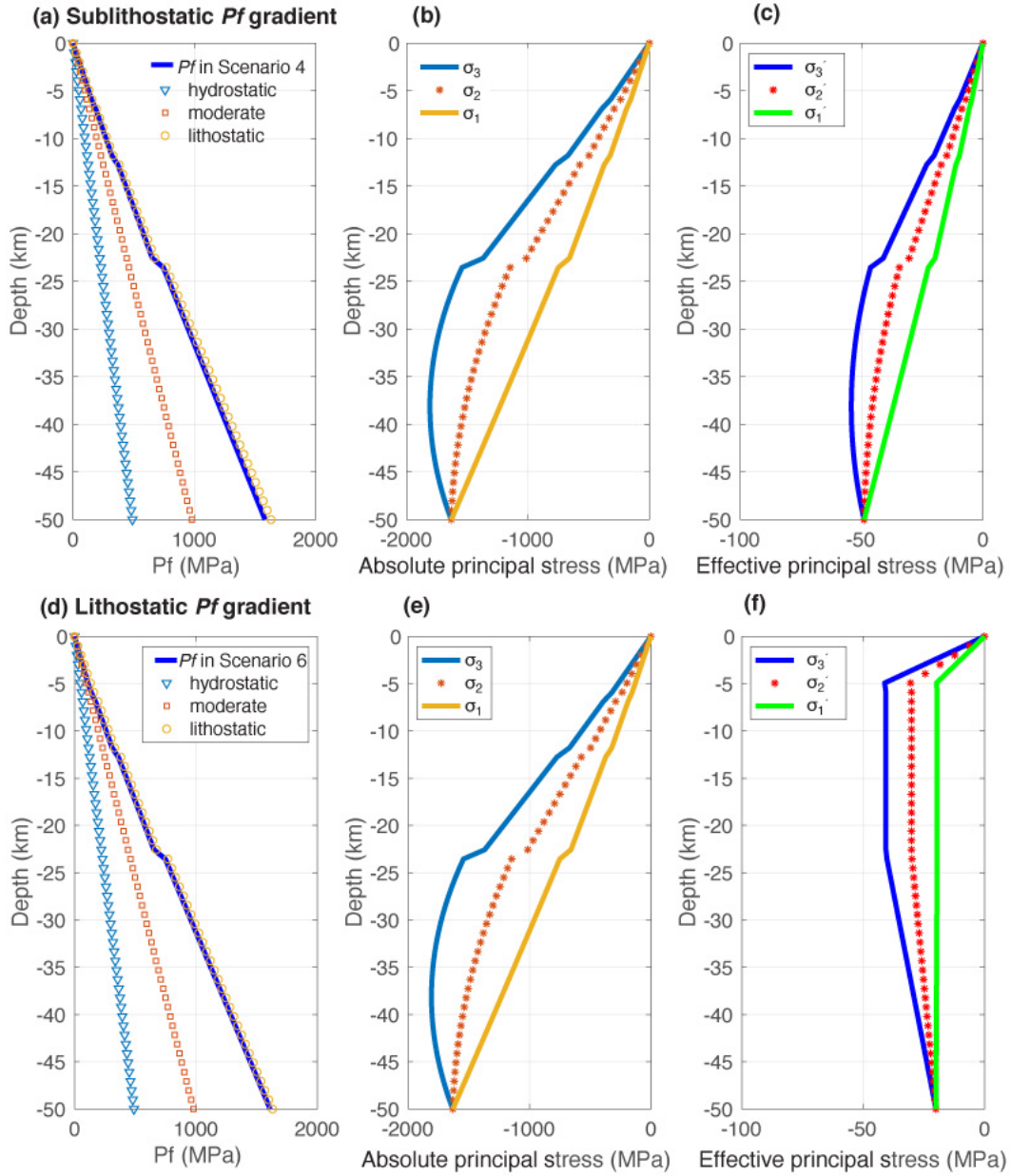


**Figure 2.** (a) Sublithostatic  $P_f$  gradient in Scenario 4 in comparison with hydrostatic, moderate and lithostatic pressure gradients. (b) The resulting absolute and (c) effective principal stresses for Scenario 4. (d) Lithostatic  $P_f$  gradient in Scenario 6 in comparison with hydrostatic, moderate and lithostatic pressure gradients. (e) The resulting absolute and (f) effective principal stresses for Scenario 6. In all six scenarios, absolute principal stresses have the same depth profiles; magnitudes scale inversely with  $P_f$  magnitude (b and e). Whether the  $P_f$  gradient is sublithostatic or lithostatic changes the effective principal stress depth profiles; magnitudes scale inversely with  $P_f$  magnitude (c and f). Stresses and  $P_f$  vary only with depth, not with horizontal location.

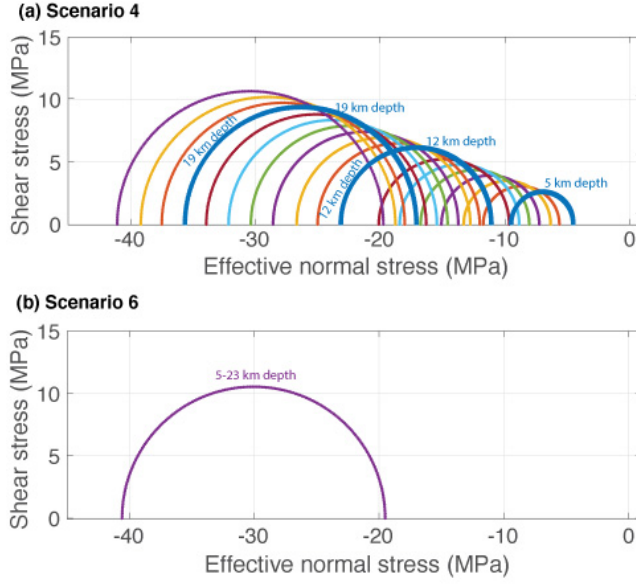


**Figure 3.** Mohr circles showing shear and effective normal stress at all possible fault orientations from 5 to 23 km depth in (a) Scenario 4 and (b) Scenario 6. As shown for Scenario 4 here, the sublithostatic  $P_f$  gradient in scenarios 1-4 causes the stresses to increase with depth (to the left). Stress magnitude ranges widen progressively from Scenario 3 to Scenario 2 to Scenario 1, but the pattern is the same. As shown for Scenario 6 here, the lithostatic  $P_f$  gradient in scenarios 5 and 6 causes the stresses to be constant with depth. The stress magnitudes are larger in Scenario 5, but remain constant with depth. Below 23 km, the differential stress is tapered to zero in all scenarios (not shown).

**Table 2.** Initial conditions for all scenarios. Mean values are averaged across the entire fault. Scenarios 1 to 4 have sublithostatic  $P_f$  gradients, while scenarios 5 and 6 have lithostatic  $P_f$  gradients.

Scenario	$P_f$ level (% of $\sigma_v^a$ )	$P_f$ parameterization	mean $\tau_s^b$ (MPa)	mean $\tau_n'^c$ (MPa)
1	low (31%)	$0.31\sigma_v$	101	-506
2	moderate (62%)	$0.62\sigma_v$	54	-277
3	high (93%)	$0.93\sigma_v$	10	-52
4	very high (97%)	$0.97\sigma_v$	4	-22
5	high (93%)	$\sigma_v - 42$ MPa	11	-47
6	very high (97%)	$\sigma_v - 20$ MPa	5	-22

<sup>a</sup>lithostatic (vertical) stress)

<sup>b</sup>initial shear traction

<sup>c</sup>initial effective normal traction

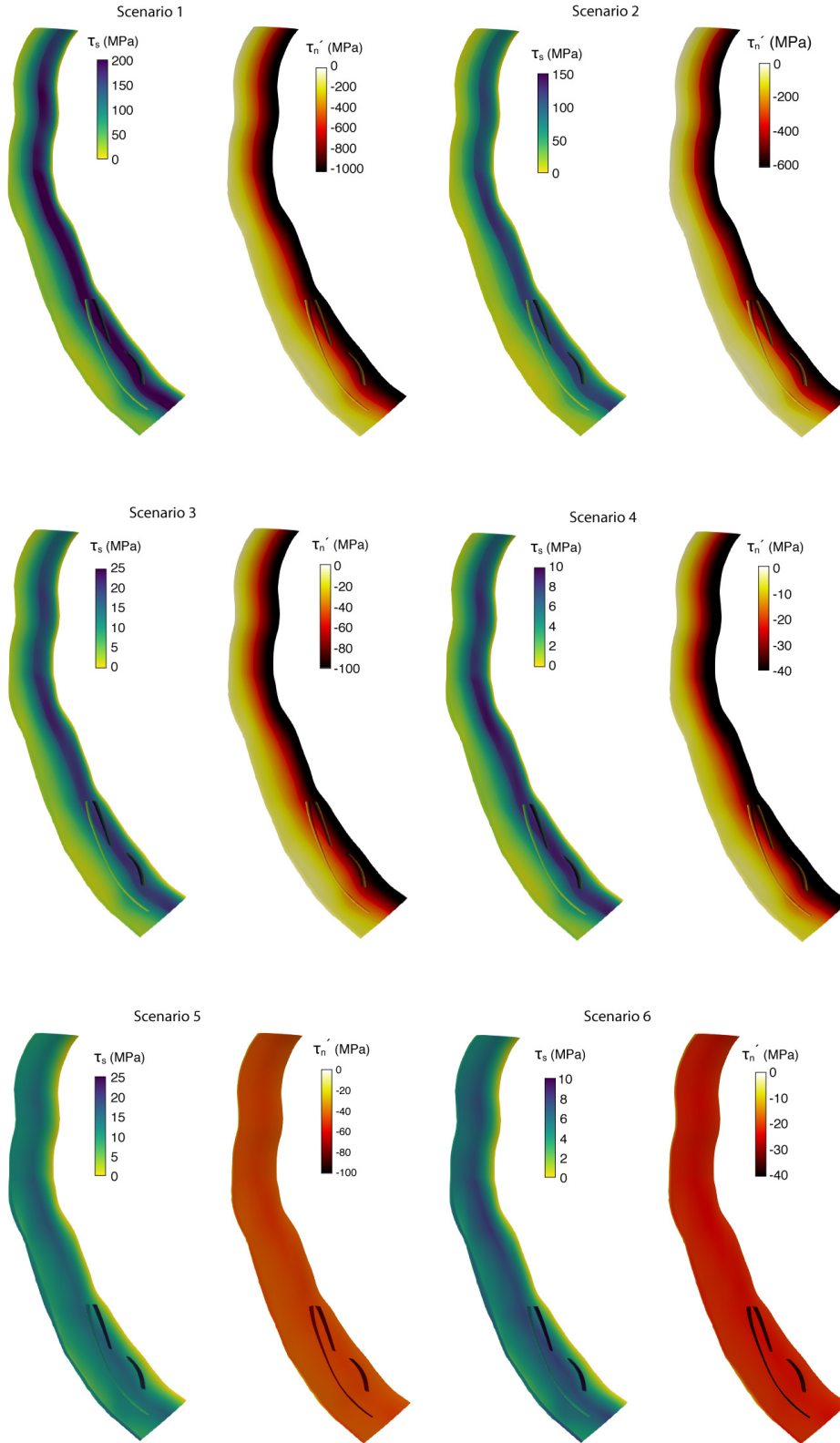


**Figure 4.** Initial shear traction ( $\tau_s$ ) and effective normal traction ( $\tau'_n$ ) on the megathrust in Scenarios 1 to 6. For each fault image, the shallowest part of the megathrust, near the seafloor, is to the left and the deepest part at 50 km depth is to the right. Note the depth-dependent  $\tau'_n$  in scenarios 1 to 4 with sublithostatic  $P_f$  gradients applied versus the nearly constant  $\tau'_n$  in scenarios 5 and 6 with lithostatic  $P_f$  gradients. Both  $\tau_s$  and  $\tau'_n$  vary with the non-planar fault geometry up to  $\approx 5$  MPa.

269 along the megathrust and splay faults below 10 km depth, but  $c$  linearly increases to 15 MPa  
 270 from 10 km to 0 km depth. Due to topography, the intersection of the fault and the seafloor  
 271 ranges between 3 and 5 km depth, so maximum  $c$  values on the faults at the seafloor range  
 272 from 8-11 MPa. For further discussion of  $c$ , please see Section 5.1 and Appendix B.

273 We assign  $\mu_s = 0.4$  to all faults in all scenarios. Borehole estimates of stress in up-  
 274 per crustal rocks suggest that rocks follow Byerlee's law with  $\mu_s = 0.6$  to 1.0 (Townend  
 275 & Zoback, 2000, 2004; Suppe, 2014). Our choice of  $\mu_s = 0.4$  is motivated by the lithol-  
 276 ogy of the shallow megathrust characterized by high, clay-rich sediment input that is pro-  
 277 gressively strengthened by dehydration and compaction near the megathrust (Hüpers  
 278 et al., 2017). Our choice to keep  $\mu_s$  constant across all faults and all scenarios allows us  
 279 to here focus on the effects of  $P_f$  magnitude and depth gradient.

280 We apply a linear slip-weakening friction law (e.g., Andrews, 1976) to represent dy-  
 281 namic weakening of a fault after failure.  $\mu_s$  decreases to the coefficient of dynamic fric-  
 282 tion,  $\mu_d$ , over the slip-weakening distance,  $D_c$ . After weakening, the dynamic strength  
 283 of the fault during slip,  $T_{fd}$ , is given by:

$$T_{fd} = -\mu_d \tau'_n \quad (3)$$

284 We assign  $\mu_d = 0.1$  and use a constant value of  $D_c = 0.8$  m. The rupture continues to  
 285 propagate as long as  $\tau_s$  locally exceeds  $T_{fs}$  and a fault continues to slip as long as suf-  
 286 ficient strain energy is available. Note that  $\tau_s$  at the rupture front is typically higher than  
 287 the initial  $\tau_s$ , so statically stronger parts of a fault may fail after the rupture initiates  
 288 elsewhere.

## 289 4 Results

### 290 4.1 Earthquake source characteristics

291 Table 3 summarizes average characteristics of the earthquakes in each scenario. As  
 292 pore fluid pressure ( $P_f$ ) increases from low to very high, the moment magnitude ( $M_w$ )  
 293 decreases, as do mean cumulative slip, peak slip rate ( $PSR$ ), mean dynamic stress drop  
 294 ( $\Delta\tau_s$ ) and rupture velocity ( $Vr$ ). This reflects our here chosen set-up, in which both shear  
 295 and effective normal tractions scale inversely with  $P_f$ .  $M_w$  of the earthquakes in scenar-  
 296 ios 1 and 2 are unrealistically large, which supports the conjecture by Saffer and Tobin  
 297 (2011) that pore fluid is likely overpressured everywhere along the seismogenic megath-  
 298 rust. Further details about scenarios 1 and 2 are given in Appendix C.  $M_w$  for the earth-  
 299 quakes in Scenarios 3 to 6 are reasonable for a rupture area the size of the Sumatra earth-  
 300 quake (Strasser et al., 2010), thus, we focus on the results for these four scenarios in the  
 301 following. Videos of the slip rate evolving along the megathrust during each of these sce-  
 302 narios are available by link from Appendix C.

303 In all four scenarios, an initially crack-like rupture develops into sharp, boomerang-  
 304 shaped rupture pulses propagating along-arc on the megathrust. Each pulse consists of  
 305 multiple rupture fronts, which are caused by reflected waves and head waves generated  
 306 at structural interfaces and the complex free surface (Huang et al., 2014). We note that  
 307 pulse-like rupture is here not caused by self-healing due to the dynamics of fault strength  
 308 (Gabriel et al., 2012), but due to geometric constraints (Weng & Ampuero, 2019). Fig-  
 309 ure 5 compares slip,  $PSR$ ,  $\Delta\tau_s$  and  $Vr$  on the megathrust at the end of the earthquakes  
 310 in scenarios 3-6. All three splay faults incorporated into the base model are dynamically  
 311 activated in all scenarios. In general, they slip an order of magnitude less than the megath-  
 312 rust.

313 The magnitude of  $P_f$  inversely affects average cumulative slip, while its gradient  
 314 (sublithostatic or lithostatic) influences the slip distribution on the megathrust (Figure 5).  
 315 As  $P_f$  increases from high in Scenario 3 to very high in Scenario 4, mean slip decreases

**Table 3.** Earthquake characteristics averaged across the megathrust

Scenario	$M_w$	mean slip (m) <sup>a</sup>	mean $PSR$ (m/s) <sup>b</sup>	mean $\Delta\tau_s$ (MPa) <sup>c</sup>	mean $Vr$ (m/s) <sup>d</sup>
1	10.2	470	75	79	4765
2	9.9	235	46	42	4246
3	9.3	26	10	8	3025
4	9.0	8	5	3	2370
5	9.4	36	11	7	3203
6	9.1	10	6	3	2624

<sup>a</sup>cumulative slip <sup>b</sup>peak slip rate <sup>c</sup>dynamic stress drop <sup>d</sup>rupture velocity

316 from 26 m to 8 m. This is reflected in the decrease in earthquake moment magnitude  
317 from  $M_w$  9.3 in Scenario 3 to  $M_w$  9.0 in Scenario 4. The slip is similarly distributed in  
318 both scenarios, with maximum slip in the middle of the fault in the down-dip direction.  
319 Slip is highest in the center of the fault along strike. Likewise, as  $P_f$  increases from high  
320 in Scenario 5 to very high in Scenario 6, mean slip decreases from 36 m to 10 m and moment  
321 magnitude decreases from  $M_w$  9.4 to  $M_w$  9.1.

322 Mean slip and  $M_w$  are similar in scenarios with the same  $P_f$  magnitude, but dif-  
323 ferent depth gradients, e.g. in scenarios 3 and 5 and in scenarios 4 and 6. However, in  
324 scenarios 5 and 6, in which the  $P_f$  gradient is lithostatic and effective normal stress is  
325 constant with depth, maximum slip is shifted up-dip relative to the locations of max-  
326 imum slip in scenarios 3 and 4, in which the  $P_f$  gradient is sublithostatic and constant  
327 effective normal stress increases with depth. Slip to the trench only occurs in Scenario  
328 5, and slip is limited at the trench in scenarios 3, 4 and 6. We discuss this further in Sec-  
329 tion 5.1 and Appendix E).

330 As with cumulative slip, peak slip rate  $PSR$  in these scenarios decreases as  $P_f$  mag-  
331 nitude increases and the  $P_f$  gradient influences its distribution along the megathrust.  
332 Mean  $PSR$  is 10 m/s in Scenario 3 with high  $P_f$  and 5 m/s in Scenario 4 with very high  
333  $P_f$ . Mean  $PSR$  is 11 m/s in Scenario 5 with high  $P_f$  and decreases to 6 m/s in Scenario  
334 6 with very high  $P_f$ . Comparing across  $P_f$  gradients, we see that scenarios 3 and 5 and  
335 scenarios 4 and 6 have similar mean  $PSR$  values, but maximum  $PSR$  occurs below 35 km  
336 depth in scenarios 3 and 4 and above 15 km in scenarios 5 and 6. Thus, relative to depth-  
337 dependent effective normal stress under sublithostatic  $P_f$  conditions, assuming a litho-  
338 static  $P_f$  gradient resulting in constant effective normal stress with depth shifts max-  
339 imum  $PSR$  up-dip (Figure 5). In addition, more of the megathrust experiences high  $PSR$   
340 in Scenario 6 relative to Scenario 4, though maximum values are lower in Scenario 6.

341 We measure the mean dynamic stress drop ( $\Delta\tau_s$ ) as the average change in shear  
342 traction ( $\tau_s$ ) from the initial value to the dynamically reached value at the end of the  
343 earthquake. As for mean slip and  $PSR$ ,  $P_f$  has an inverse relationship with mean  $\Delta\tau_s$ .  
344 Mean  $\Delta\tau_s$  is 8 MPa in Scenario 3 and 7 MPa in Scenario 5, and 3 MPa in both scenar-  
345 ios 4 and 6. The distribution of  $\Delta\tau_s$  varies with the  $P_f$  depth gradient. In scenarios 3  
346 and 4,  $\Delta\tau_s$  is larger along the deeper fault, reaching values of 15 MPa and 7 MPa, re-  
347 spectively, below 30 km depth (Figure 5). In scenarios 5 and 6,  $\Delta\tau_s$  is relatively constant  
348 along the central fault in the down-dip direction. The highest values are farther up-dip  
349 near 20 km depth, at 12 MPa and 5 MPa in these scenarios, respectively. In all scenar-  
350 ios,  $\Delta\tau_s$  is largest along the central portion of the fault along strike.

351 In contrast to the other earthquake characteristics, there is little variation in the  
352 distribution of  $Vr$  with  $P_f$  depth gradient. However, an increase in  $P_f$  magnitude over-  
353 all causes a decrease in average rupture velocity,  $Vr$ , from 3025 m/s in Scenario 3 to 2370 m/s  
354 in Scenario 4 and from 3206 m/s in Scenario 5 to 2624 m/s in Scenario 6. Mean  $Vr$  is

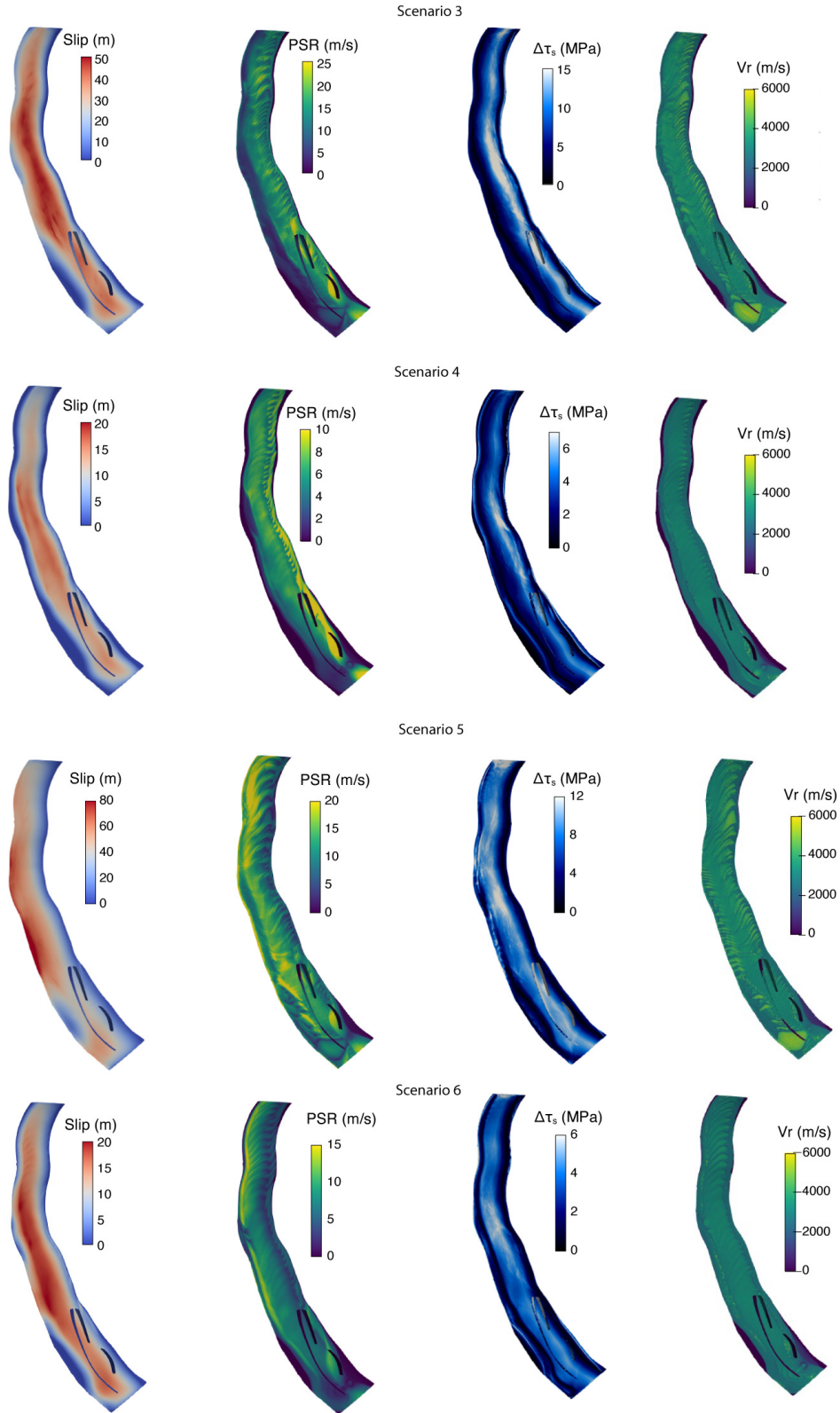


**Figure 5.** For Scenarios 3 to 6: cumulative slip, peak slip rate ( $PSR$ ), dynamic stress drop ( $\Delta\tau_s$ ), and rupture velocity ( $V_r$ ) on the megathrust. For each fault image, the shallowest part of the fault is to the left and the deepest part (at 50 km depth) is to the right. A version with alternative colorbar limits that are set for comparison across scenarios is included as Figure C2.

**Table 4.** Pre- and post-earthquake mean principal stress orientations<sup>a</sup>

Scenario		$\sigma_3$ trend	plunge	$\sigma_2$ trend	plunge	$\sigma_1$ trend	plunge
all	pre	225±0°	7±0°	315±0°	7±0°	90±0°	80±0°
3	post	184±41°	7±5°	258±56°	36±26°	53±34°	51±24°
4	post	193±33°	7±5°	253±60°	22±18°	48±37°	66±16°
5	post	197±64°	9±11°	257±33°	44±20°	70±16°	42±19°
6	post	197±35°	9±6°	277±40°	22±16°	68±20°	64±16°

<sup>a</sup> calculated in vertical slice and in hanging wall only (see Figure 6)

355 lower in Scenario 3 relative to Scenario 5, and lower in Scenario 4 relative to Scenario  
 356 6, suggesting that average  $Vr$  increases under conditions of constant versus depth-dependent  
 357 effective normal stress.

358 In all scenarios, average  $Vr$  is sub-Rayleigh relative to the lower velocity subduc-  
 359 tion channel surrounding the megathrust slip interface ( $V_s = 3500$  m/s, Table 1). While  
 360  $Vr$  is below Rayleigh wave speed across most of the megathrust in all scenarios, excep-  
 361 tions of supershear rupture appear i) propagating up-dip from the hypocenter at close  
 362 to P-wave speed triggered by energetic nucleation and ii) in the form of localized and  
 363 relatively slow supershear fronts excited before the sub-Rayleigh rupture front at sev-  
 364 eral isolated locations. In Scenario 5, where  $Vr$  is highest out of all scenarios, at these  
 365 isolated locations  $Vr \approx 70\%$  of P-wave speed.  $Vr$  that exceeds the S-wave speed, but  
 366 remains lower than the P-wave speed, agrees with inferences and modeling for earthquake  
 367 rupture in damaged fault zones (Harris & Day, 1997; Huang et al., 2016; Bao et al., 2019;  
 368 Oral et al., 2020).

## 369 4.2 Post-earthquake stress field

370 The dynamic rupture model utilized in these scenarios permits investigation of the  
 371 post-earthquake absolute stress field. We compare principal stress orientations and rel-  
 372 ative magnitudes along a cross-section of the central part of the rupture in scenarios 3  
 373 to 6 (see inset in Figure 6a). Figure 6a shows the orientations of the principal stresses  
 374 ( $\sigma_3 < \sigma_2 < \sigma_1$ , compression is negative) before the earthquake for all scenarios and  
 375 Figure 6b shows the orientations after dynamic earthquake rupture in Scenario 4. The  
 376 post-earthquake stress orientations for scenarios 3, 5 and 6 are shown in Figure F1. We  
 377 summarize the post-earthquake stress orientations for all scenarios in stereonet focused  
 378 on the hanging wall and footwall regions close to the fault in Figure 6c. We compare the  
 379 mean orientations of the principal stresses in the hanging wall before and after the earth-  
 380 quake in Table 4 and report average rotations in Table 5. We note that the reported changes  
 381 in orientation from before to after the earthquake are “apparent” rotations and do not  
 382 account for a principal stress switching locations with another principal stress due to mag-  
 383 nitude changes. These apparent rotations are similar to rotations inferred from earth-  
 384 quake data, for which information is available only before and after an earthquake.

385 In all scenarios, the principal stresses rotate more in the hanging wall than in the  
 386 footwall. In the hanging wall across all scenarios, the trend of  $\sigma_3$  rotates counterclock-  
 387 wise by 28-40° toward parallel with megathrust strike, while its plunge remains shallow  
 388 at 7-9°.  $\sigma_2$  rotates counterclockwise by 38-63° and its plunge steepens by 15-37°.  $\sigma_1$  ro-  
 389 tates counterclockwise by 20-42° and its plunge shallows by 14-38° from near-vertical  
 390 (80°) to moderate (42-66°).

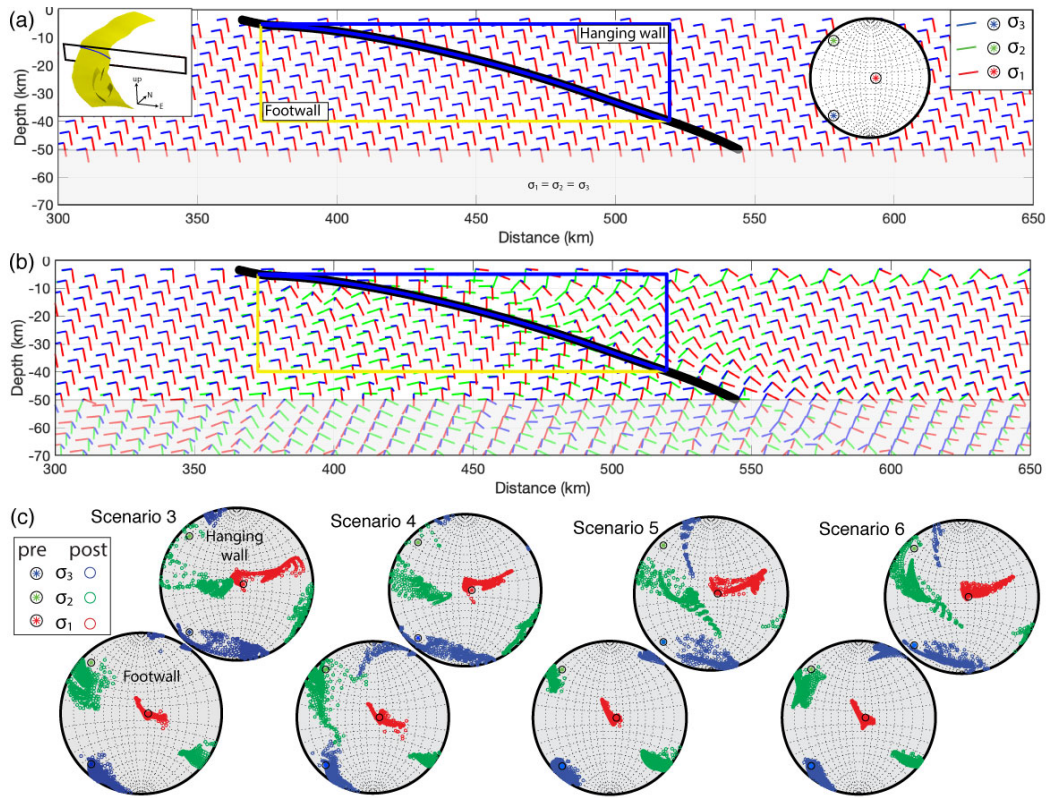


**Figure 6.** (a) Orientations of the principal stresses before the earthquake for all scenarios.  $\sigma_2$  vectors are behind  $\sigma_3$  vectors. The black line is the megathrust profile. Blue and yellow lines outline the hanging wall and footwall regions analysed in (c). The left inset shows the cross-section location through the model volume near the fault (yellow). The right inset shows the stereonet of pre-earthquake principal stresses. (b) Orientations after the dynamic earthquake rupture in Scenario 4, with a sublithostatic  $P_f$  gradient. (c) Stereonets of post-earthquake principal stress orientations in Scenario 4. Hanging wall and footwall regions are outlined in (a) and (b).

**Table 5.** Apparent mean coseismic principal stress rotations<sup>a</sup>

Scenario	$\sigma_3$ rotation	$\sigma_2$ rotation	$\sigma_1$ rotation
3	46±18°	50±20°	34±20°
4	36±18°	38±18°	21±11°
5	55±16°	58±17°	39±17°
6	36±18°	36±20°	19±14°

<sup>a</sup>calculated in vertical slice through hanging wall only (see Figure 6)

391 In all scenarios,  $\sigma_2$  and  $\sigma_3$  have similar mean apparent rotations and rotate more  
 392 than the minimum principal stress,  $\sigma_1$ . The mean principal stress rotations in the hang-  
 393 ing wall summarized in Table 5 vary with the magnitude of pore fluid pressure ( $P_f$ ). As  
 394  $P_f$  increases from Scenario 3 to Scenario 4 and from Scenario 5 to Scenario 6, mean ro-  
 395 tations of each principal stress decrease in accordance with decreasing stress drop. Sce-  
 396 narios 4 and 6 have very similar apparent rotations for each principal stress, suggesting  
 397 that the choice of  $P_f$  depth gradient does not affect the amount of rotation when the  $P_f$   
 398 magnitude is very high (97% of the lithostatic pressure,  $\sigma_v$ ). Such similarity is not ap-  
 399 parent when comparing scenarios 3 and 5. Mean rotations in Scenario 5 are the largest  
 400 of all scenarios, which we attribute this to the high fault slip at the trench in this sce-  
 401 nario.

402 To better understand the post-earthquake stress field, we also consider the effec-  
 403 tive principal stress magnitudes relative to one another. This is important to the stress  
 404 rotation analysis, because magnitudes of two principal stresses that move closer to one  
 405 another approach the condition for switching orientations, allowing for a larger amount  
 406 of heterogeneity in the post-earthquake stress field. Figure 7 shows the maximum dif-  
 407 ferential stress,  $\sigma'_{d13} = \sigma'_1 - \sigma'_3$ , before and after the dynamic earthquake ruptures in  
 408 scenarios 3 to 6. Prior to each earthquake, the distributions of  $\sigma'_{d13}$  depend on the gra-  
 409 dient in  $P_f$ . Scenarios 3 and 4 have the same depth-dependent pattern of  $\sigma'_{d13}$ , but the  
 410 maximum  $\sigma'_{d13}$  values in each scenario differ by up to 30 MPa. Similarly, scenarios 5 and  
 411 6 have the same pattern, which shows relatively constant values to 25 km depth before  
 412 tapering begins, but the maximum  $\sigma'_{d13}$  values in each scenario differ by up to 20 MPa.

413 Table 6 summarizes the mean values of all three differential stresses in the hang-  
 414 ing wall:  $\sigma'_{d13}$ ,  $\sigma'_{d12} = \sigma'_1 - \sigma'_2$  and  $\sigma'_{d23} = \sigma'_2 - \sigma'_3$ . As  $P_f$  increases from Scenario 3 to  
 415 Scenario 4 and from Scenario 5 to Scenario 6, pre-earthquake  $\sigma'_{d13}$  averages in the hang-  
 416 ing wall decrease by  $\approx 20$  MPa. In each scenario,  $\sigma'_{d12}$  equals  $\sigma'_{d23}$  before the earthquake,  
 417 as  $\sigma_2$  is initially set to be halfway between  $\sigma_3$  and  $\sigma_1$ . Pre-earthquake, the magnitudes  
 418 of these differential stresses differ from Scenario 3 to Scenario 4 and from Scenario 5 to  
 419 Scenario 6 by  $\approx 10$  MPa.

420 In the plots of the post-earthquake  $\sigma'_{d13}$  distributions in Figure 7, contours indi-  
 421 cate the amount and direction (increase or decrease) of the change in  $\sigma'_{d13}$ .  $\sigma'_{d13}$  decreases  
 422 in the footwall in all scenarios along the central fault, but increases below the bottom  
 423 of the fault.  $\sigma'_{d13}$  decreases in the hanging wall in all scenarios, except near the end of  
 424 the fault at depth. Decreases in  $\sigma'_{d13}$  in the hanging wall are larger in scenarios 3 and  
 425 5, reaching 15 MPa and above over larger areas near the megathrust, corresponding to  
 426 the larger slip in these scenarios relative to scenarios 4 and 6, respectively. Decreases in  
 427  $\sigma'_{d13}$  reach 10 MPa in scenario 4 and 5 Mpa in scenario 6.

428 In all scenarios, there are larger changes in average  $\sigma'_{d23}$  than in average  $\sigma'_{d12}$  due  
 429 to the larger coseismic decrease in the magnitude of  $\sigma'_3$  relative to the decreases in  $\sigma'_1$   
 430 and  $\sigma'_2$  (Table 5). The closeness of  $\sigma'_2$  and  $\sigma'_3$  before the earthquake therefore controls

**Table 6.** Differential stress before and after the earthquake<sup>a</sup>

Scenario	$\sigma'_{d13}$ pre <sup>b</sup>	$\sigma'_{d13}$ post	$\sigma'_{d12}$ pre	$\sigma'_{d12}$ post	$\sigma'_{d23}$ pre	$\sigma'_{d23}$ post
3	34±14	27±10	17±7	15±7	17±7	12±4
4	15±6	12±5	7±3	7±3	7±3	5±2
5	42±5	31±5	21±3	18±7	21±3	12±5
6	20±2	14±4	10±1	9±2	10±1	5±3

<sup>a</sup>calculated in vertical slice through hanging wall only (see Figure 6)

<sup>b</sup> maximum differential stress,  $\sigma'_{d13} = \sigma'_1 - \sigma'_3$  (MPa)

431 the amount of apparent post-seismic stress rotation here, and how likely these two prin-  
 432 cipal stresses are to switch locations. In contrast,  $\sigma'_2$  and  $\sigma'_1$  have less apparent rotation,  
 433 making them less likely to swap orientations.

## 434 5 Discussion

435 We present 6 earthquake scenarios that vary in  $P_f$  magnitude and depth gradient  
 436 in order to explore the dynamic effects of different pre-earthquake  $P_f$  levels and distri-  
 437 butions in subduction zones. The model structure and input are consistent with condi-  
 438 tions for the 2004 Sumatra-Andaman earthquake, using a base model following (Uphoff  
 439 et al., 2017). We first discuss how the scenario earthquakes reflect observations of that  
 440 event, as well as more general observations of earthquakes along megathrusts. Then, we  
 441 discuss inferences from these scenarios relevant to fault mechanics. We analyze further  
 442 the stress rotations from before to after these scenario earthquakes and compare them  
 443 to observations following the 2004 Sumatra earthquake.

### 444 5.1 Earthquake characteristics

445 Pre-earthquake conditions are not easily constrained by observations, here along  
 446 the Sumatra-Andaman trench or elsewhere in the world. However, the observational match-  
 447 ing of the base model by Uphoff et al. (2017) used here gives an ideal starting point to  
 448 explore the effects of  $P_f$  on earthquake dynamics. In addition, the 3D physics-based for-  
 449 ward modeling approach unifies the pre-earthquake conditions together with the earth-  
 450 quake dynamics to arrive at physically consistent earthquake characteristics, a capabil-  
 451 ity of large-scale and geometrically complex computational models highlighted by Ulrich  
 452 et al. (2022).

453 To first order, scenarios 3 and 6 produce earthquakes with moment magnitudes sim-  
 454 ilar to those inferred for the Sumatra earthquake of  $M_w$  9.1 to 9.3 (Shearer & Bürgmann,  
 455 2010), while the Scenario 4 earthquake is just below this range at  $M_w$  9.0 and the Sce-  
 456 nario 5 earthquake is just above this range at  $M_w$  9.4 (Table 3). Maximum slip values  
 457 from kinematic source inversions compiled by Shearer and Bürgmann (2010) range up  
 458 to a maximum value of  $\approx 35$  m, suggesting that the slip in the Scenario 5 earthquake,  
 459 which averages 36 m, is too large. Seno (2017) estimates a mean stress drop of 3 MPa  
 460 for this earthquake, which is matched by those for scenarios 4 and 6. In contrast, sce-  
 461 narios 3 and 5 have mean dynamic stress drops that are more than twice this value. The  
 462 mean rupture velocities in scenarios 4 and 6, respectively 2370 m/s and 2624 m/s, are  
 463 similar to the rupture velocity of 2500 m/s inferred by Ammon et al. (2005) for the 2004  
 464 earthquake. In contrast, scenarios 3 and 5 both have mean  $Vr$  exceeding 3000 m/s.

465 Furthermore, Seno (2017) estimates a subducted sediment thickness of  $1.57 \pm 0.12$  km  
 466 near Simeulue, in the southern region of the 2004 earthquake, which is high in compar-

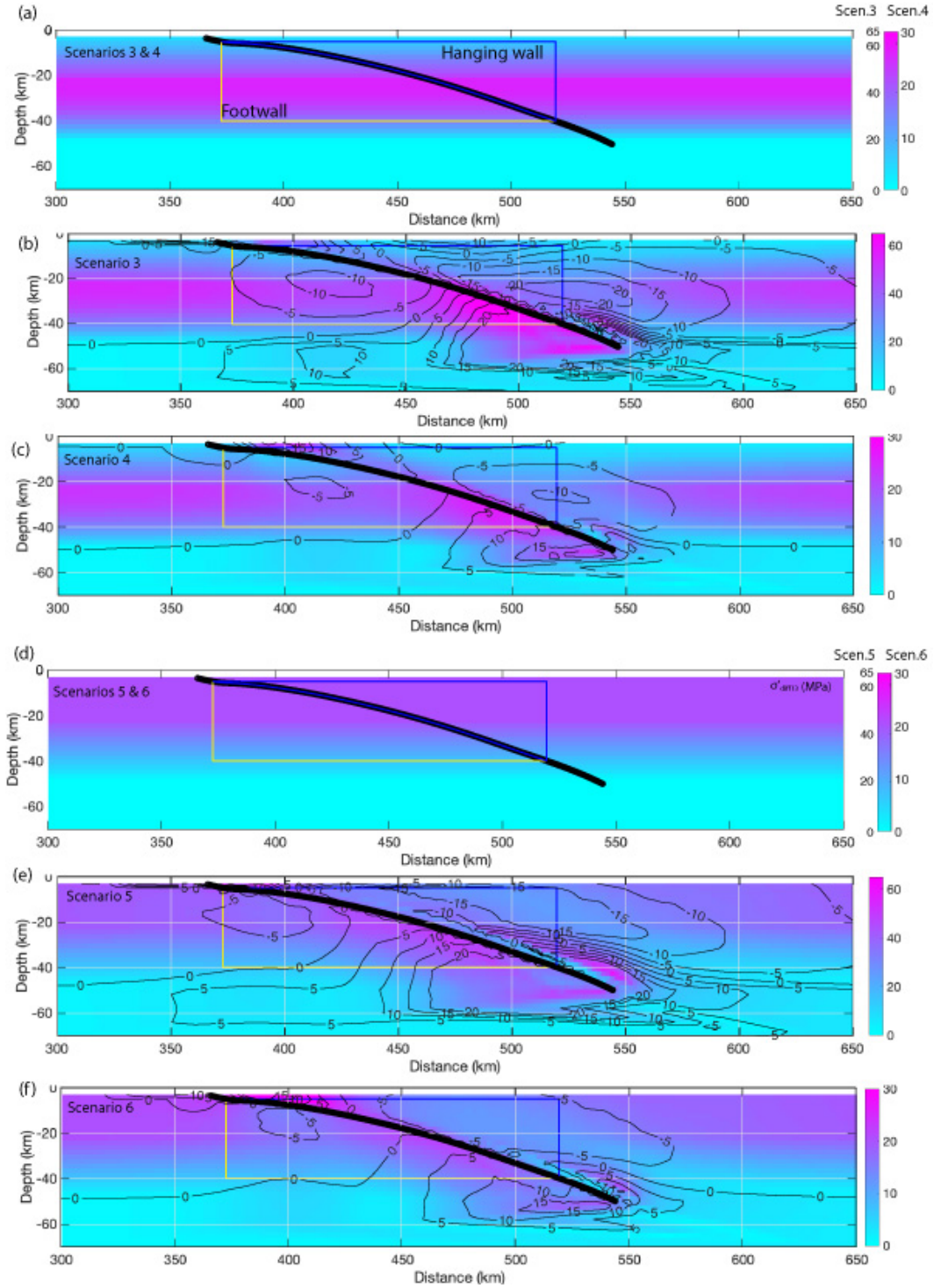


**Figure 7.** Cosismic change in maximum effective differential stress ( $\sigma'_{d13}$ ) (a) before the earthquake in scenarios 3 and 4, (b) after the earthquake in Scenario 3, (c) after the earthquake in Scenario 4, (d) before the earthquake in scenarios 5 and 6, (e) after the earthquake in Scenario 5, and (f) after the earthquake in Scenario 6. Contours show change in  $\sigma'_{d13}$  from pre- to post-earthquake. Location is as shown in inset in Figure 6.

467 ison with other subduction zones. Correlation between subducted sediment thickness,  
 468 stress drop and  $P_f$  by Seno (2017) suggests that  $P_f$  should be high and stress drop should  
 469 be low in this earthquake, as in both scenarios 4 and 6. This highlights the earthquakes  
 470 in scenarios 4 and 6 as more realistic.

471 Scenarios 4 and 6 both have very high  $P_f$  at 97 % of the lithostatic stress ( $\sigma_v$ ), but  
 472 differ in the way that  $P_f$  is acting on the curved fault system. In Scenario 4,  $P_f$  follows  
 473 a sublithostatic depth gradient and the effective normal traction ( $\tau'_n$ ) increases with depth.  
 474 In Scenario 6, following theoretical work by (Rice, 1992),  $P_f$  follows the lithostatic gra-  
 475 dient, maintaining a constant difference to  $\sigma_v$ . As a result,  $\tau'_n$  is close to constant with  
 476 depth along most of the megathrust (varying only by up to 5 MPa due to variations in  
 477 fault geometry). The good performance of both scenarios 4 and 6 relative to observa-  
 478 tions of the 2004 Sumatra earthquake suggests that megathrust earthquakes may occur  
 479 under very high pre-earthquake  $P_f$  resulting in low  $\tau'_n$ . Scenario 6 emerges as the event  
 480 that best matches observations, as Scenario 4 has lower slip that results in a  $M_w$  9.0 event,  
 481 smaller than the  $M_w$  9.1 to 9.3 2004 earthquake (Shearer & Bürgmann, 2010). This sug-  
 482 gests that megathrust earthquakes may occur under conditions of a lithostatic  $P_f$  depth  
 483 gradient, resulting in relatively constant  $\tau'_n$  along the megathrust.

484 These scenarios also are representative of variable conditions that may be present  
 485 along a single megathrust at the same point in time, due to spatial variations in  $P_f$  mag-  
 486 nitude and/or gradient. Such variations in  $P_f$  are one possible mechanism of conceptual  
 487 seismic asperities, inducing heterogeneity in dynamic fault motion (Lay et al., 2012; Bürgmann,  
 488 2018). Sediments and high  $P_f$  have been proposed as important mechanisms aiding sta-  
 489 ble sliding along geometric, frictional and rheological barriers, while (less effectively) ther-  
 490 mal pressurization may provide a mechanism for stress-roughening slip events (Wibberley  
 491 & Shimamoto, 2005; Barbot, 2019; Perry et al., 2020; Gabriel et al., 2020). Our presented  
 492 scenarios serve as building blocks for future along-arc heterogeneous models, that may  
 493 be calibrated with site-specific friction and pore-fluid measurements to constrain dynam-  
 494 ically plausible megathrust strength and  $P_f$  gradients. For example, we find that very  
 495 high  $P_f$  leading to constant effective normal stress with depth produces a stress drop on  
 496 the megathrust that is nearly constant with depth and pushes peak slip rate up-dip on  
 497 the megathrust. Also, earthquake magnitude and mean cumulative slip are larger for an  
 498 equal or lower mean stress drop under these conditions. For a given subduction zone or  
 499 megathrust event, such detailed conditions may be constrained by geodetic, geological,  
 500 or tsunami observations (e.g. Ulrich et al., 2022).

501 High or very high  $P_f$  that follows the lithostatic gradient favours higher slip at shal-  
 502 lower depths, thus increasing the importance of near-trench strength and constitutive  
 503 behavior in determining megathrust hazard. Widespread and high amplitude slip to the  
 504 trench only occurs in Scenario 5, and slip is limited at the trench in scenarios 3, 4 and  
 505 6. In all scenarios, near-trench behavior is influenced by the choice of on-fault cohesion,  
 506  $c$ , which is used as a proxy for near-trench behavior that we do not model explicitly here,  
 507 such as velocity-strengthening during slip in shallow sediments (e.g. Kaneko et al., 2008)  
 508 and the energy lost to rock yielding around the megathrust (off-fault plasticity, e.g. Gabriel  
 509 et al., 2013).  $c$  is the same in all scenarios, but its relative contribution to the static fault  
 510 strength increases as  $P_f$  increases and  $\tau'_n$  decreases (Eq.2, Figure 4). Models that aim  
 511 to capture natural co-seismic near-trench processes (e.g. Dunham et al., 2011; Ma, 2012;  
 512 Lotto et al., 2019; Ma & Nie, 2019; Ulrich et al., 2022) can further discriminate govern-  
 513 ing factors of near-trench behavior (see also Appendix E). Specifically, Ulrich et al. (2022)  
 514 focus on near-trench behavior during the 2004 Sumatra earthquake and its influence on  
 515 the subsequent Indian Ocean tsunamis.

516 Next, we look to general observations of stress drop from earthquakes on the sub-  
 517 ducting interface to further decipher between scenarios. Allmann and Shearer (2009) re-  
 518 port depth-dependent stress drops when data is considered separately by region. Uchide  
 519 et al. (2014) find an increasing stress drop from 30–60 km depth in a spectral decom-

520 position analysis of smaller events occurring before the 2011 Tohoku earthquake. How-  
 521 ever, Bilek and Lay (2018) and Denolle and Shearer (2016) report very weak correlation  
 522 between stress drop and depth. Abercrombie et al. (2021) re-evaluate previous studies  
 523 based on the spectral decomposition method and show that when trade-offs between at-  
 524 tenuation and depth-dependent sources are accounted for, the correlation between stress  
 525 drop and depth from previous studies decreases and, in some cases, disappears altogether.  
 526 We determine the dynamic stress drop on the megathrust in each scenario, which dif-  
 527 fers slightly from these observationally inferred values, but remains well within obser-  
 528 vational and methodological uncertainties. We find that dynamic stress drop varies more  
 529 with depth in scenarios 3 and 4 (up to 15 MPa), due to the depth-dependent effective  
 530 normal traction resulting from the sublithostatic  $P_f$  gradient (Figure 5). In contrast, stress  
 531 drop varies up to only 7 MPa in scenarios 5 and 6, where effective normal traction is rel-  
 532 atively constant along the megathrust resulting from the lithostatic  $P_f$  gradient. Thus,  
 533 a correlation between stress drop and depth is more consistent with high  $P_f$  following  
 534 a sublithostatic gradient, while a low dependence of stress drop on depth is more con-  
 535 sistent with high  $P_f$  following a lithostatic gradient. Should these end-member condi-  
 536 tions be present in different locations along a single megathrust, deciphering a depen-  
 537 dence of stress drop on depth observationally will be difficult. On the other hand, well-  
 538 constrained observations of depth-dependent versus depth-constant stress drops of small  
 539 events may differentiate between locations of sublithostatic (scenarios 1-4) versus litho-  
 540 static (scenarios 5 and 6)  $P_f$  gradients along megathrusts.

541 Under a lithostatic  $P_f$  gradient, the effective normal stress is constant and the ef-  
 542 fective normal tractions ( $\tau'_n$ ) are relatively constant, but variations of  $\approx 5$  MPa still arise  
 543 due to variations in fault geometry. Bletery et al. (2016) attribute the location and ex-  
 544 tent of the 2004 Sumatra earthquake rupture to a region of relatively homogeneous megath-  
 545 rust shear strength. Homogeneity of  $\tau'_n$ , and therefore of fault shear strength in these  
 546 scenarios, is promoted by high  $P_f$  that follows the lithostatic gradient with depth. Such  
 547 homogeneous shear strength is more likely to be exceeded simultaneously over large ar-  
 548 eas, leading to the large earthquakes events observed in subduction zones. However, it  
 549 is interesting to note that conditions of relatively homogeneous  $\tau'_n$  and shear strength  
 550 may actually emphasize the influence of geometry on earthquake behavior, as geometry  
 551 becomes the main control on shear strength variation along the megathrust. Both ef-  
 552 fects may be explored in future work focusing on variations in megathrust geometry com-  
 553 plexity and cycles of fault slip (e.g. Perez-Silva et al., 2021) and by relaxing our assump-  
 554 tion of a constant shear to effective normal traction ratio.

## 555 5.2 Inferences from these scenarios relevant to fault mechanics

556 Here, we consider the scenarios in light of inferences about fault mechanics, begin-  
 557 ning with the initial shear traction ( $\tau_s$ ) on the fault, then discussing effective normal trac-  
 558 tion ( $\tau'_n$ ) magnitudes and variation with depth.  $\tau_s$  scales with  $\tau'_n$  from scenario to sce-  
 559 nario and the distribution of  $\tau_s/\tau'_n$  is the same in all scenarios (Figure B1). A static fric-  
 560 tion coefficient of 0.4 is applied in all scenarios.

561 From force-balance studies, Lamb (2006) finds that the crust above 7 out of 9 stud-  
 562 ied subduction zones sustains an average  $\tau_s$  of 7-15 MPa. This includes Sumatra, with  
 563 an average  $\tau_s$  of 15.2 MPa (Lamb, 2006, Table 5), which is similar to the mean  $\tau_s$  prior  
 564 to rupture on the megathrust in scenarios 3 and 5. Brodsky et al. (2020, Fig. 6) constrain  
 565  $\tau_s$  on the shallow part of the Tohoku megathrust prior to the 2011 Tohoku earthquake  
 566 at  $\approx 1.7$  MPa using a friction coefficient derived from low-velocity friction experiments.  
 567 Yao and Yang (2020) find the shear strength of the megathrust that ruptured in the 2012  
 568 Nicoya earthquake to be less than 7.5 MPa on average. In combination with observed  
 569 low stress drops of subduction megathrust events (Sibson & Rowland, 2003), low dynamic  
 570 shear stresses during earthquake rupture (e.g. less than 1 MPa, Choy & Boatwright, 1995;  
 571 Pérez-Campos & Beroza, 2001) also support low  $\tau_s$  on megathrusts prior to earthquakes,

572 although this may include additional weakening from a variety of dynamic effects (Gao  
573 & Wang, 2014).

574 In this suite of 6 scenarios, more reasonable earthquakes emerge at higher pre-earthquake  
575  $P_f$  magnitudes and average initial  $\tau_s$  values in scenarios 3 to 6 range from 5 to 11 MPa  
576 (Table 2). Thus  $P_f$  higher than approximately 93% of the lithostatic gradient is consis-  
577 tent with inferences of low initial shear stress on the megathrust. As suggested by the  
578 analysis in Section 5.1, scenarios 4 and 6 produce the most realistic earthquakes, sup-  
579 porting  $P_f$  averaging at 97% of the lithostatic stress ( $\sigma_v$ ) and consistent with mean  $\tau_s$   
580 on the megathrust of 4-5 MPa. There are exceptions to inferences of low initial  $\tau_s$ , how-  
581 ever. Lamb (2006) estimates values of 18.3 and 36.7 MPa on the Chile and Tonga megath-  
582 rusts, respectively, while depth-dependence is inferred for the Tohoku and northern Hiku-  
583 rangi megathrusts with values ranging up to 80 MPa (Gao & Wang, 2014; K. Wang et  
584 al., 2019). These values are more consistent with scenarios 3 and 5.

585 In all scenarios, the megathrust is moderately strong, with a static friction coef-  
586 ficient of 0.4. However, the low shear strengths ( $T_{fs}$ , Eq. 2) of the megathrust in the pre-  
587 ferred scenarios can be used to classify the megathrust as weak. The megathrust also  
588 is dynamically weak, with friction dropping to 0.1 during sliding.

589 In these scenarios, high  $P_f$  leads to low maximum differential stress (and a low devi-  
590 ator stress magnitude) and therefore to low  $\tau_s$  along the megathrust. However, low  
591 maximum differential stress (and a low deviatoric stress magnitude) can occur indepen-  
592 dently of  $P_f$ , for example from absolute principal stresses that are close to one another  
593 in magnitude. We assume a least compressive principal stress,  $\sigma_1$ , in our scenarios that  
594 is close to  $\sigma_v$ . The other two principal stresses must be larger in magnitude in a thrust  
595 faulting regime, but are more difficult to constrain.  $\sigma_3$  could vary from what we choose,  
596 which would then change  $\tau_s$  on the megathrust as well as the average  $\tau_s$  associated with  
597 a particular  $P_f$ . More complicated stress conditions also are likely. For example, we choose  
598 to set  $\sigma_2$  midway between  $\sigma_1$  or  $\sigma_3$ , but this is not necessarily the case in nature. In ad-  
599 dition, principal stress magnitudes may vary in magnitude or orientation along the megath-  
600 rust, both laterally and with depth. Past earthquakes may leave heterogeneous shear trac-  
601 tions on the megathrust and  $P_f$  likely varies spatially in the vicinity of the megathrust  
602 (Heise et al., 2017). Close to the fault, there is field evidence of stress rotations within  
603 the damage zone that vary the principal stress orientations from those in the remote field  
604 (Faulkner et al., 2006) and this condition is supported by theory (Rice, 1992). It will be  
605 interesting to relate stress complexity with  $P_f$  and additional along-arc heterogeneity  
606 in future work.

### 607 5.3 Off-fault results

608 It has been suggested that principal stress rotations are promoted by complete or  
609 near-complete stress drops that permit principal stresses to swap orientations (Brodsky  
610 et al., 2017, 2020; X. Wang & Morgan, 2019). However, by connecting 2-D stress rota-  
611 tions to the ratio of stress drop over pre-earthquake deviatoric stress magnitude, Hardebeck  
612 (2012, 2015) shows that partial stress release may generate moderate rotations. Scenar-  
613 ios 3 and 5 experience the largest rotations, but have larger initial differential stresses  
614 and larger post-earthquake differential stresses as well. The larger rotations in these sce-  
615 narios appear to scale with fault slip and stress drop, both of which are larger than in  
616 scenarios 4 and 6. X. Wang and Morgan (2019) attribute observed changes in stress ori-  
617 entations following the 2011 Tohoku earthquake to rapid weakening of a statically strong  
618 fault with  $\mu_s$  in the range of 0.3 - 0.6. K. Wang et al. (2019) attribute rotations to a weak  
619 megathrust, with a low effective friction coefficient (0.032) and low shear stress in the  
620 forearc leading to low shear traction on the megathrust. These theories are compatible  
621 with one another, if the megathrust is considered to be statically strong, but dynami-

622 cally weak, in terms of its dynamic friction coefficient, and if  $P_f$  is high. This is supported  
 623 by the scenarios presented here, with  $\mu_s=0.4$  and  $\mu_d = 0.1$ .

624 None of the scenarios results in a complete stress drop and yet we find that the post-  
 625 seismic stress field supports a variety of potential aftershock focal mechanisms. In all sce-  
 626 narios,  $\sigma_3$  rotates toward parallel with megathrust strike and its plunge remains more  
 627 or less unchanged, while the plunge of  $\sigma_2$  increases and the plunge of  $\sigma_1$  decreases. This  
 628 post-seismic stress state supports a variety of aftershock mechanisms, including strike-  
 629 slip faulting where  $\sigma_1$  plunges more shallowly relative to  $\sigma_2$ , and reverse faulting where  
 630  $\sigma_2$  plunges more shallowly relative to  $\sigma_1$ . Of 13  $M_w$  6 or larger aftershocks with focal  
 631 mechanisms solutions in the GCMT catalog (Dziewonski et al., 1981; Ekström et al., 2012)  
 632 occurring along the central rupture within five years of the 2004 Sumatra mainshock (through  
 633 December 27, 2009), 8 are reverse and 5 are strike-slip. We define the central rupture  
 634 here as the region from  $5^\circ$  to  $9^\circ$  latitude,  $91^\circ$  to  $97.3^\circ$  longitude, and 0-50 km depth, cor-  
 635 responding to the location of the fault-perpendicular slice in Figure 6. Out of 125  $M_w$  5  
 636 or larger aftershocks occurring within 1 month of the mainshock in the same region, 63  
 637 have strike-slip focal mechanisms, while 29 have reverse, 31 have normal mechanisms and  
 638 2 cannot be categorized.

639 At Sumatra, Hardebeck (2012) finds rotations of the maximum compressive prin-  
 640 cipal stress, which we call  $\sigma_3$ , relative to the megathrust and in the two-dimensional (2D)  
 641 plane perpendicular to the megathrust, to be up to  $\approx 42^\circ$  and increasing from South to  
 642 North. Along the central rupture (zone B in Hardebeck, 2012), average  $\sigma_3$  rotation is  
 643  $26\pm 13^\circ$ . Using the 2D solution proposed by Hardebeck and Hauksson (2001), the ratio  
 644 of the mean earthquake stress drop to the magnitude of the deviatoric stress,  $\Delta\tau_s/\sigma_{dev}$ ,  
 645 can be estimated as a function of the pre-earthquake angle of  $\sigma_3$  to the megathrust and  
 646 its rotation. At Sumatra specifically, Hardebeck (2012) finds that this ratio varies from  
 647 0.6 along the southern part of the rupture to 0.8 along the central and northern part of  
 648 the rupture. This implies that 60-80% of the pre-earthquake deviatoric stress magnitude  
 649 along the megathrust was relieved by the earthquake. The apparent rotations of  $\sigma_3$  along  
 650 the central rupture in these scenarios (Table 5) are of similar magnitudes to those de-  
 651 termined from data (Hardebeck, 2012), ranging from  $36^\circ$  to  $55^\circ$ , but are predominantly  
 652 in the horizontal plane. We also find similar ratios of  $\Delta\tau_s$  to  $\sigma_{dev}$  in these scenarios, of  
 653 0.6 in Scenarios 4, 5 and 6 and of 0.7 in Scenario 3. We do not see correspondence be-  
 654 tween differences in  $\Delta\tau_s/\sigma_{dev}$  and the amount of  $\sigma_3$  rotation (Table 5), but note that  
 655 this analysis is not directly comparable to the 2D analysis by Hardebeck (2012), as  $\sigma_3$   
 656 rotates out of the plane perpendicular to the megathrust in these scenarios.

657 Post-earthquake stress and aftershock focal mechanism heterogeneity would be fur-  
 658 ther promoted in a model incorporating a heterogeneous initial stress field. In these sce-  
 659 narios, a laterally-constant, depth-dependent regional stress tensor is applied, so  $P_f$  and  
 660 the resulting effective stress field are the same near to and far from the megathrust be-  
 661 fore the earthquake. Such similar on- and off-fault stresses are not likely in nature. Away  
 662 from the megathrust, secondary faulting, the earthquake history, and material contrasts  
 663 likely produce stress heterogeneities (I. v. Zelst et al., 2020). Heterogeneity in the mag-  
 664 nitude of the effective intermediate principal stress,  $\sigma'_2$ , relative to the maximum and min-  
 665 imum effective principal stresses also would contribute to aftershock heterogeneity, by  
 666 making it easier for different faulting regimes to be activated. For example, as we note  
 667 in Section 4.2, the magnitude of  $\sigma'_2$  relative to the other two effective principal stresses  
 668 controls the ability for  $\sigma'_2$  to switch places with  $\sigma'_1$  or  $\sigma'_3$ , thus affecting postseismic stress  
 669 rotations. In addition, dynamic effects that decouple conditions on- and off-fault, such  
 670 as thermal pressurization (Noda, 2008; Noda et al., 2009) during which  $P_f$  increases rapidly  
 671 due to reduced pore pressure diffusion in the fault zone during slip, may allow low ef-  
 672 fective normal tractions on the megathrust, even while a different stress state persists  
 673 away from the fault. Considering more complex initial stress conditions off the fault and  
 674 decoupling on- and off-fault stresses are clear next steps for this work.

## 6 Conclusions

We analyse the effects of pore fluid pressure ( $P_f$ ) magnitude and gradient on pre-earthquake stress conditions and earthquake dynamics using 3D high-performance computing enabled, physics-based dynamic rupture models that permit geometrically complex faults. The 6 scenarios presented, based on the 2004  $M_w$  9.1 Sumatra-Andaman earthquake, have  $P_f$  that varies from hydrostatic to lithostatic under sublithostatic versus lithostatic gradients. These result, respectively, in either depth-dependent or constant effective normal stress near the megathrust and splay faults. As  $P_f$  increases in these scenarios, moment magnitude, cumulative slip, peak slip rate, dynamic stress drop and rupture velocity all decrease. A lithostatic  $P_f$  gradient causes relatively constant effective normal tractions on the megathrust, moves peak slip and peak slip rate up-dip, and produces a more constant stress drop across the megathrust. This is consistent with theoretical analysis and observations inferring that the stress drops of smaller earthquakes in subduction zones are only weakly depth-dependent.

In comparison with a range of observations, we identify two preferred scenarios that both support the presence of very high coseismic pore fluid pressure on average over the ruptured area (here 97 % of the lithostatic pressure). These have low mean shear and effective normal traction magnitudes of 4-5 MPa and 22 MPa, respectively. The mean dynamic stress drop for these two scenario earthquakes is 3 MPa and the mean rupture velocity is 2400-2600 m/s, similar to observations of the 2004 Sumatra-Andaman earthquake. Although comparison with observations of the 2004 earthquake cannot conclusively differentiate between these two preferred scenarios, a lithostatic  $P_f$  gradient, which causes constant normal stress near the megathrust, may be the theoretically more plausible condition under very high  $P_f$  magnitudes. On weak megathrusts, in terms of the low static shear strength and low dynamic friction during rupture, where  $P_f$  follows the lithostatic gradient, near-trench strength and constitutive behavior are crucially important for megathrust hazard, as peak slip and peak slip rate occur at shallower depths.

Mean apparent rotations of the principal stresses in the hanging wall decrease as  $P_f$  magnitude increases, but do not vary with  $P_f$  gradient. Scenarios with the largest rotations have larger initial differential stress and larger post-earthquake differential stress as well. The larger rotations in these scenarios scale with fault slip and stress drop. Along the central rupture, maximum compressive stress rotations in the hanging wall average  $36\pm 18^\circ$  toward trench-parallel in the two preferred scenarios and the minimum principal stress rotates from near-vertical toward a shallower plunge. This post-earthquake stress field is consistent with the heterogeneous aftershocks observed following the Sumatra earthquake.

Variations in  $P_f$  are one possible mechanism of conceptual seismic asperities, and our analysis may serve as guidance for future along-arc heterogeneous models. In addition, this work has implications for tsunami hazard, as the  $P_f$  gradient is shown to influence the location of maximum slip and slip rate. Under conditions of a lithostatic  $P_f$  gradient, relatively constant effective normal tractions down-dip along the megathrust push maximum slip and slip rate toward the surface.

## Appendix A Model mesh resolution

Dynamic rupture simulations must resolve the cohesive zone width  $\Lambda$ , which spans the part of the fault across which shear stress decreases from its static to its dynamic value. In heterogeneous dynamic rupture simulations,  $\Lambda$  can vary considerably across the fault in dependence of initial stress, frictional properties and propagation distance. Since  $\Lambda$  also changes dynamically across the fault, the number of elements per median  $\Lambda$  can also vary significantly across the fault for a given simulation. Yet, we here highlight selected findings from Wollherr et al. (2018), that allow for better understanding of how

725 the numerical accuracy of the ADER-DG scheme of SeisSol in resolving on fault time-  
 726 dependent parameters is affected by mesh size and polynomial degree. By comparing the  
 727 rupture arrival time, peak slip rate time, final slip and the peak slip rate averaged across  
 728 363 receivers with respect to a reference solution, Wollherr et al. (2018) show that er-  
 729 rors are globally decreasing with mesh refinement and increasing polynomial degree. Seis-  
 730 Sol resolves shear and normal stress and effective friction according to a friction law ev-  
 731 erywhere at the fault at  $(p + 2)^2$  Gaussian quadrature points inside each fault element  
 732 triangle, with  $p$  being the polynomial degree (and  $p = 3$  in this study leading to 4th order  
 733 order accuracy in space and time, as measured in the L2 norm, of the ADER-DG scheme  
 734 for seismic wave propagation).

735 In this study, we ensure that we resolve the median  $\Lambda$ , estimated at 1 km for Sce-  
 736 nario 3, 1.6 km for Scenario 4, 0.9 km for Scenario 5, and 1.5 km for Scenario 6. In as-  
 737 sessing sufficient resolution, we follow Wollherr et al. (2018) and Day et al. (2005). Day  
 738 et al. (2005) is defining a dynamic rupture solution to be sufficiently close to the refer-  
 739 ence solution once the RMS errors reached the following thresholds: lower than 0.2 %  
 740 for rupture arrival time, lower than 7 % for peak slip rate and lower than 1 % for final  
 741 slip. We calculate  $\Lambda$  as the difference in distance between the rupture front arrival time  
 742 and the first point in time at which shear stresses reach their dynamic value across the  
 743 fault. The minimum  $\Lambda$  (approximated at the 15th percentile of all measured) varies across  
 744 the scenarios as follows: 346 m in Scenario 3, 540 m in Scenario 4, 469 m in Scenario 5  
 745 and 627 m in Scenario 6. By analyzing scenarios 3 and 6, with the longest and short-  
 746 est  $\Lambda$ , we find that the errors for rupture arrival range from 0.09-0.20 % and for final slip  
 747 range from 0.68-1.2 % across these four scenarios, which are sufficiently small with re-  
 748 spect to the findings by Day et al. (2005). The expected errors for peak slip rate are higher,  
 749 ranging from 8.9-17 %, above the 7 % recommended by Day et al. (2005), however Ramos  
 750 et al. (2021) verify with higher resolution models that even with expected errors above  
 751 7 % for peak slip rate, megathrust slip is not affected in comparable SeisSol dynamic rup-  
 752 ture models.

## 753 Appendix B Prestress ratio and on-fault frictional cohesion

754 The relative prestress ratio,  $R$ , is the ratio of the fault stress drop ( $\tau_s - T_{fd}$ ) to the  
 755 breakdown strength drop ( $T_{fs} - T_{fd}$ ), where  $\tau_s$  is the initial shear traction,  $T_{fs}$  is the static  
 756 fault strength and  $T_{fd}$  is the dynamic fault strength during sliding (Aochi & Madariaga,  
 757 2003).  $R$  varies along the megathrust with the non-planar fault geometry (Figure B1),  
 758 but is nearly the same across all scenarios since  $\tau_s/\tau'_n$  is constant across all scenarios.  
 759 The exception to this is with respect to the on-fault frictional cohesion,  $c$ .  $c$  is similar  
 760 across all scenarios, but contributes differently to  $T_{fs}$  in each scenario and this changes  
 761  $R$  slightly from scenario to scenario, particularly at shallow depths (see also Appendix Ap-  
 762 pendix E).

763 Cohesion,  $c$ , depends on local mineralogy and lithology. However,  $c$  is used here  
 764 to limit slip in the absence of near-trench behavior, using the lowest value that restricts  
 765 unrealistic slip and rupture dynamics (e.g. occurrence of supershear rupture) at the trench.  
 766 We find this to be  $c = 0.4$  MPa below 10 km depth and increasing linearly to 15 MPa  
 767 at 0 km depth (Figure B2). We tested two alternative  $c$  gradients from 0.4 MPa below  
 768 10 km to maxima of 1 MPa and 10 MPa at  $z=0$ , which lead to unrealistic near-surface  
 769 behavior. As these scenarios do not capture the constitutive behavior of shallow sedi-  
 770 ments in the near-trench region, we do not draw conclusions about near-trench behav-  
 771 ior or about realistic  $c$  values from these scenarios (see also Appendix E). Ulrich et al.  
 772 (2022) takes the work in this direction by incorporating slip-strengthening behavior near  
 773 the seafloor, as well as off-fault plasticity, into models of the 2004 Sumatra-Andaman earth-  
 774 quake.

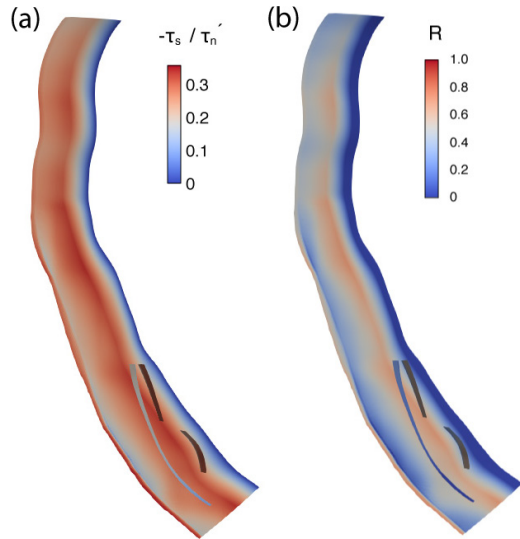


**Figure B1.** (a) The ratio of the initial shear traction to effective normal traction ( $\tau_s/\tau'_n$ ) varies depending on the megathrust orientation relative to the local stress tensor, but the distribution on the megathrust is the same across all scenarios. (b) The prestress ratio,  $R$ , is shown here for Scenario 4, but is similar in all scenarios.

775 When the fault is in tension and effective normal stress equals zero, the fault strength  
 776 is equal to  $c$ . This is because tensile stresses are treated in SeisSol to prevent fault open-  
 777 ing following a standard approach in the dynamic rupture community (Harris et al., 2009,  
 778 2018). This procedure treats tension on the fault the same as if the effective normal stress  
 779 equals zero.

## 780 Appendix C Scenarios 1 and 2 earthquakes

781 Slip, peak slip rate, dynamic stress drop and rupture velocity are shown in Figure  
 782 C1 for Scenarios 1 and 2, which have low and moderate  $P_f$ , respectively.

## 783 Appendix D Earthquake videos

784 We provide animations showing absolute slip rate evolving along the megathrust  
 785 during the earthquakes in scenarios 3 to 6 here: <https://doi.org/10.5281/zenodo.5914960>.

## 786 Appendix E Slip at the trench

787 Slip proceeds to the trench in Scenario 5 and reaches maximum values there, which  
 788 is clearly different from scenarios 3, 4 and 6 (Figure 5, Figure C2). A similar difference  
 789 between shallow slip in Scenario 4 and Scenario 6 is also visible in Figure 5. These dif-  
 790 ferences are due not only to  $P_f$  magnitude and depth gradient, but also to the contri-  
 791 bution of the applied on-fault cohesion,  $c$ , to static fault strength,  $T_{fs}$  (see also Appendix  
 792 B. In all scenarios,  $c$  is constant below 10 km depth and linearly increases toward the  
 793 surface above, contributing to  $T_{fs}$  according to Equation 2. The influence of  $c$  on  $T_{fs}$   
 794 increases as  $P_f$  increases and  $\tau'_n$  decreases. As a result, closeness to failure varies  
 795 near the seafloor in all scenarios. Fault strength is overcome at the trench only in Scenario  
 796 5, while slip is restricted along the top of the fault in scenarios 3, 4, and 6. This contrast

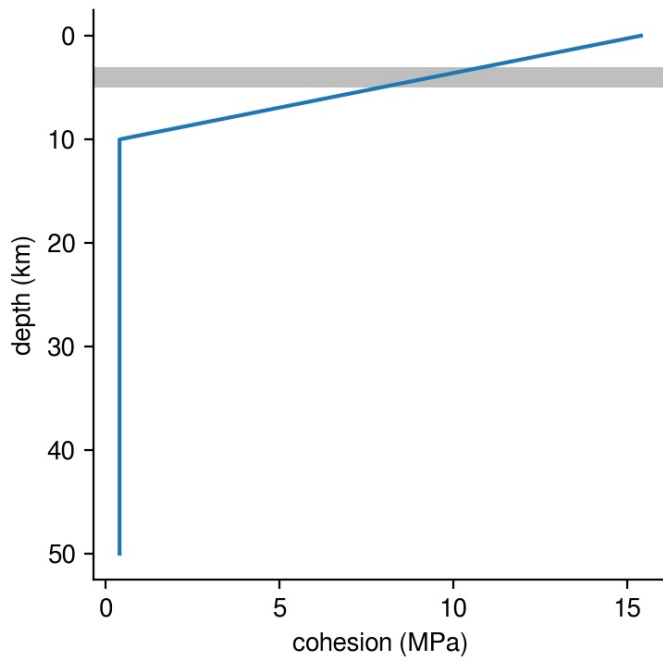


**Figure B2.** Blue line is on-fault frictional cohesion,  $c$ , which is set to 0.4 MPa below 10 km depth and increases linearly to 15 MPa at 0 km depth. Due to topography, the intersection of the fault and the seafloor ranges between 3 and 5 km depth, so maximum  $c$  values on the megathrust and splay faults at the seafloor range from 8–11 MPa. The grey line shows this intersection between fault and seafloor on average.

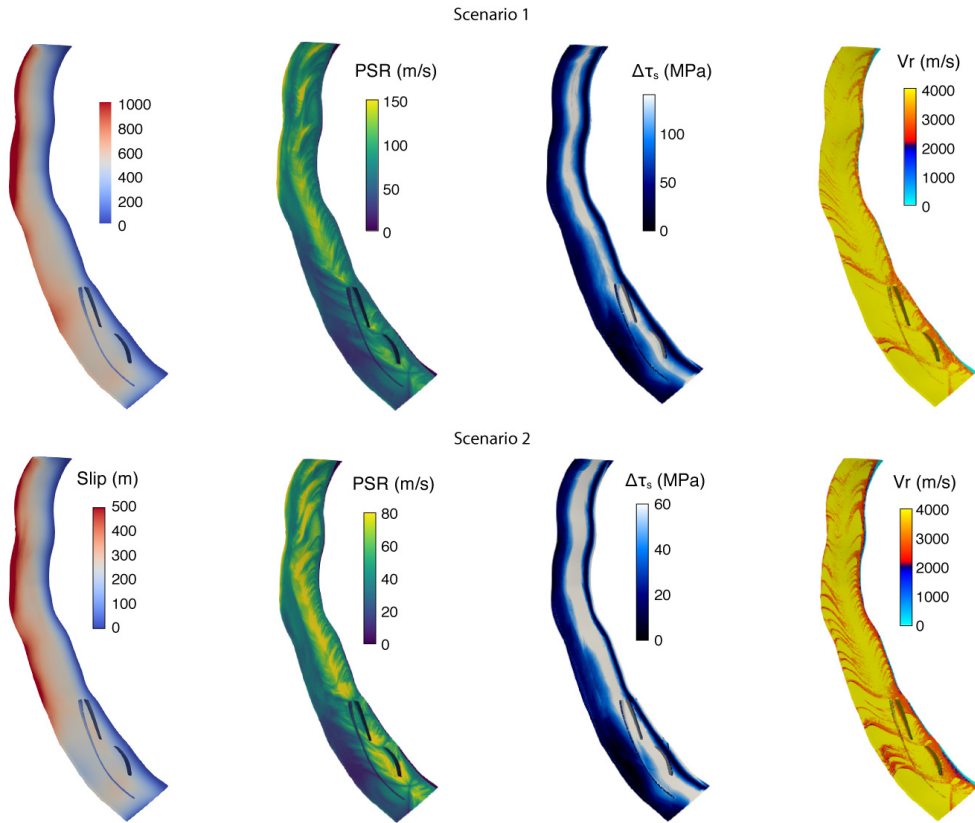


**Figure C1.** Cumulative slip, peak slip rate ( $PSR$ ), stress drop ( $\Delta\tau_s$ ) and rupture velocity ( $V_r$ ) on the megathrust in Scenarios 1 and 2. For each fault image, the shallowest part of the fault (where it intersects the seafloor) is to the left and the deepest part (at 50 km depth) is to the right.

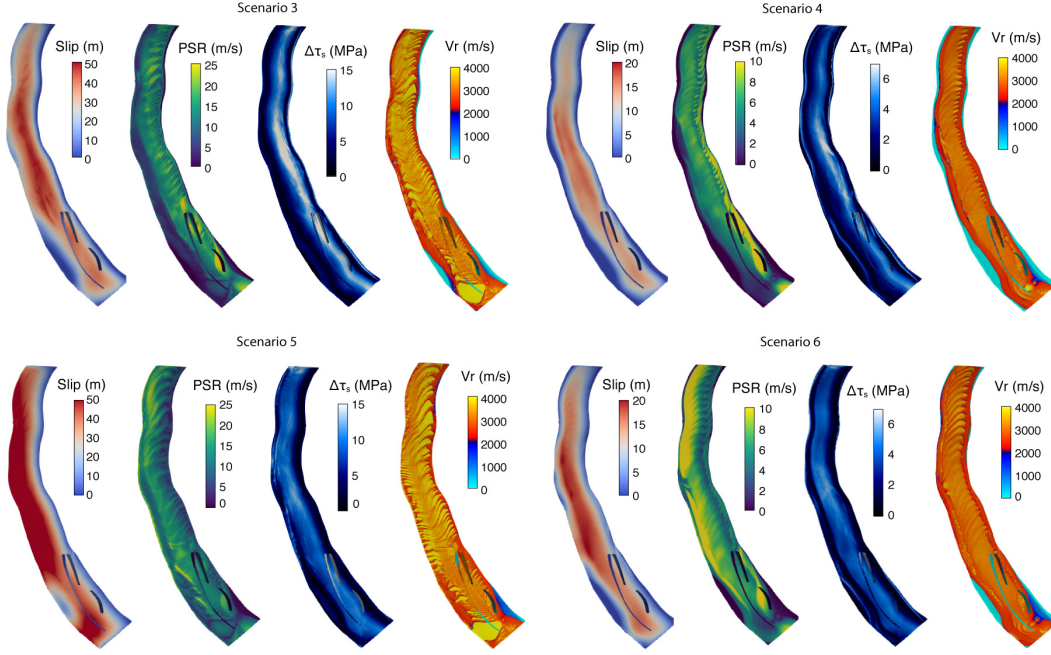


**Figure C2.** Cumulative slip, peak slip rate ( $PSR$ ), stress drop ( $\Delta\tau_s$ ) and rupture velocity ( $Vr$ ) on the megathrust for scenarios 3-6 with alternative colorbars from Figure 5 that are better for comparison across scenarios. For each fault image, the shallowest part of the fault is to the left and the deepest part (at 50 km depth) is to the right.

797 is important because it highlights both that the influence of  $c$  on slip behavior at the trench  
 798 increases as  $P_f$  increases and  $c$  becomes a larger component of  $T_{fs}$ , and that near-trench  
 799 slip is encouraged by very high  $P_f$  following a lithostatic gradient that causes conditions  
 800 of constant  $\tau'_n$  along the megathrust and pushes maximum slip and slip rate closer to  
 801 the trench. In these scenarios,  $c$  is defined as the strength of the fault in the absence of  
 802  $\tau_n$  (Equation 2) and is used as a proxy for near-trench behavior that we do not model  
 803 explicitly here, including the energy lost to damage around the megathrust (off-fault plas-  
 804 ticity, e.g. Gabriel et al., 2013) and velocity-strengthening of the fault in shallow sedi-  
 805 ments (e.g. Kaneko et al., 2008). Further study of slip behavior at the trench requires  
 806 that the appropriate physical processes near the seafloor are incorporated into the model  
 807 (e.g. Dunham et al., 2011; Ma, 2012; Lotto et al., 2019; Ma & Nie, 2019; Ulrich et al.,  
 808 2022). For example, Ulrich et al. (2022) incorporate slip strengthening and off-fault plas-  
 809 ticity of lithified shallow sediments into coupled earthquake-tsunami models of the 2004  
 810 Sumatra earthquake and Indian Ocean tsunami to study near-trench slip, seafloor dis-  
 811 placement and tsunami genesis using a coupled tsunami model.

## 812 Appendix F Post-earthquake stress field

813 Figure F1 shows the post-seismic stress field for all scenarios. While the rotation  
 814 directions are similar in all scenarios, the amount of rotation is larger in scenarios 3 and  
 815 5 than in scenarios 4 and 6. Stereonets are included in the main text (Figure 6).

## 816 Acknowledgments

817 We would like to thank Dmitry Garagash and Taras Gerya for helpful discussions, as well  
 818 as the participants of the 2019 SZ4D MCS RCN Megathrust Modeling Workshop in Eu-

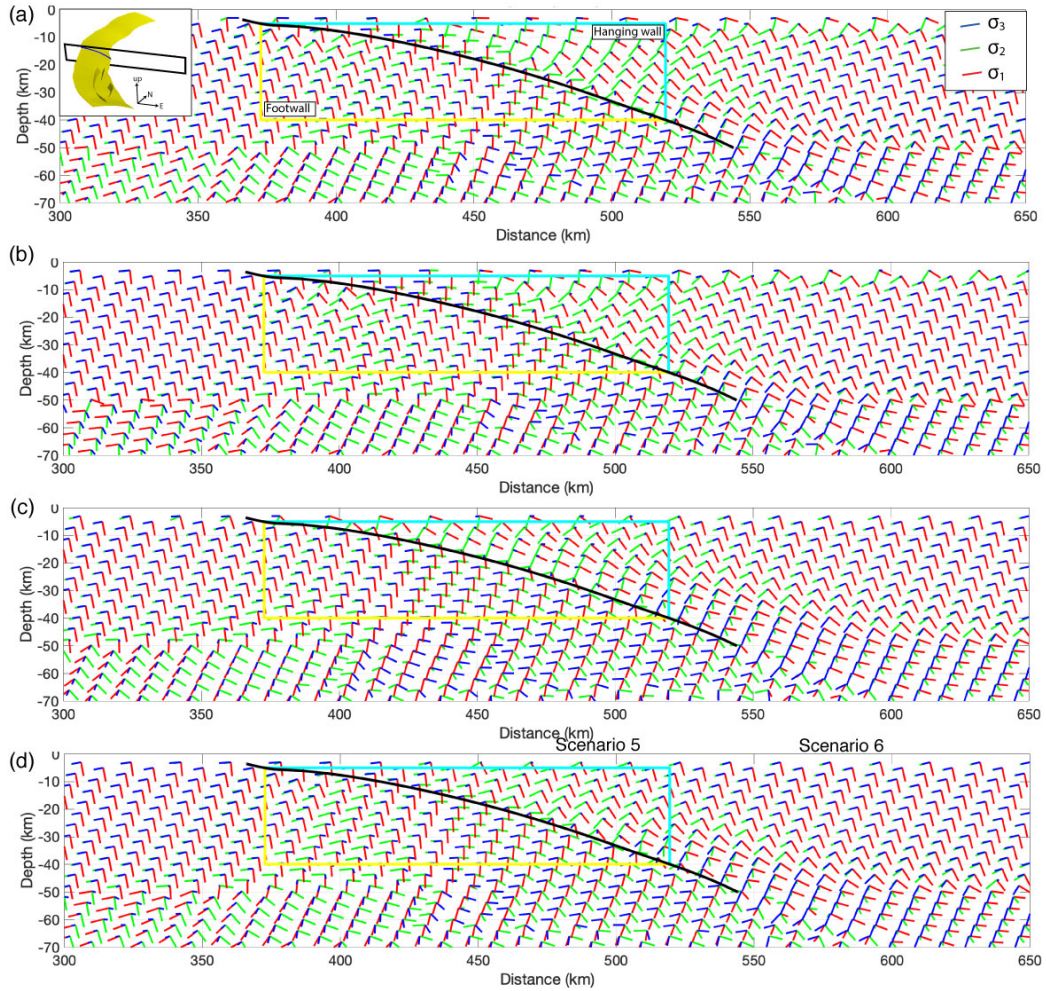


**Figure F1.** Orientations of the principal stresses after the earthquake in (a) Scenario 3, (b) Scenario 4, (c) Scenario 5 and (d) Scenario 6. Black line is the megathrust profile. Blue and yellow lines outline the hanging wall and footwall regions. Black box in left inset in (a) shows location of slice through the volume along the fault (yellow).

gene, Oregon. Simulations were conducted using the open-source software package SeisSol (DOI:10.5281/zenodo.4899349), which also is freely available at [github.com/SeisSol/SeisSol](https://github.com/SeisSol/SeisSol). All simulation input files are accessible at the Zenodo data repository: <https://doi.org/10.5281/zenodo.5914661>. The authors acknowledge funding from the Volkswagen Foundation (project “ASCETE”, grant no. 88479), the European Union’s Horizon 2020 research and innovation program (TEAR ERC Starting grant no. 852992 and ChEESE Center of Excellence, grant no. 823844), the German Research Foundation (DFG) (projects GA 2465/2-1, GA 2465/3-1), by KAUST-CRG (FRAGEN, grant no. ORS-2017-CRG6 3389.02), by KONWIHR – the Bavarian Competence Network for Technical and Scientific High Performance Computing (project NewWave), by BayLat – the Bavarian University Centre for Latin America, and by the National Science Foundation (NSF Grant No. EAR-2121666). Computing resources were provided by the Institute of Geophysics of LMU Munich (Oeser et al., 2006) and the Leibniz Supercomputing Centre (LRZ, projects no. pr63qo and pr45fi).

## References

- Abercrombie, R. E., Trugman, D. T., Shearer, P. M., Chen, X., Zhang, J., Pennington, C., ... Ruhl, C. J. (2021). Does earthquake stress drop increase with depth in the crust? *Earth and Space Science Open Archive*, 41. doi: 10.1002/essoar.10506989.1
- Allmann, B. P., & Shearer, P. M. (2009, jan). Global variations of stress drop for moderate to large earthquakes. *Journal of Geophysical Research: Solid Earth*, 114(1). doi: 10.1029/2008JB005821
- Ammon, C. J., Ji, C., Thio, H.-K., Robinson, D., Ni, S., Hjorleifsdottir, V., ... Wald, D. (2005, may). Rupture Process of the 2004 Sumatra-Andaman Earthquake. *Science*, 308(5725), 1133–1139. doi: 10.1126/science.1112260
- Andrews, D. J. (1976). Rupture propagation with finite stress in antiplane strain. *Journal of Geophysical Research (1896-1977)*, 81(20), 3575–3582. doi: 10.1029/JB081i020p03575
- Aochi, H., & Madariaga, R. (2003, jun). The 1999 Izmit, Turkey, earthquake: Nonplanar fault structure, dynamic rupture process, and strong ground motion. *Bulletin of the Seismological Society of America*, 93(3), 1249–1266. doi: 10.1785/0120020167
- Aochi, H., Poisson, B., Toussaint, R., Rachez, X., & Schmittbuhl, J. (2014, mar). Self-induced seismicity due to fluid circulation along faults. *Geophysical Journal International*, 196(3), 1544–1563. doi: 10.1093/gji/ggt356
- Audet, P., Bostock, M. G., Christensen, N. I., & Peacock, S. M. (2009). Seismic evidence for overpressured subducted oceanic crust and megathrust fault sealing. *Nature*, 457(7225), 76–78. doi: 10.1038/nature07650
- Audet, P., & Schwartz, S. Y. (2013). Hydrologic control of forearc strength and seismicity in the Costa Rican subduction zone. *Nature Geoscience*, 6(10), 852–855. doi: 10.1038/ngeo1927
- Bao, H., Ampuero, J.-P., Meng, L., Fielding, E. J., Liang, C., Milliner, C. W., ... Huang, H. (2019). Early and persistent supershear rupture of the 2018 magnitude 7.5 palu earthquake. *Nature Geoscience*, 12(3), 200–205.
- Barbot, S. (2019, oct). Slow-slip, slow earthquakes, period-two cycles, full and partial ruptures, and deterministic chaos in a single asperity fault. *Tectonophysics*, 768, 228171. doi: 10.1016/j.tecto.2019.228171
- Beeler, N. M., Thomas, A., Bürgmann, R., & Shelly, D. (2013, nov). Inferring fault rheology from low-frequency earthquakes on the San Andreas. *Journal of Geophysical Research: Solid Earth*, 118(11), 5976–5990. doi: 10.1002/2013JB010118
- Bilek, S. L., & Lay, T. (2018, aug). Subduction zone megathrust earthquakes. *Geosphere*, 14(4), 1468–1500. doi: 10.1130/GES01608.1

- 872 Bletery, Q., Thomas, A. M., Rempel, A. W., Karlstrom, L., Sladen, A., & De Bar-  
 873 ros, L. (2016, nov). Mega-earthquakes rupture flat megathrusts. *Science*,  
 874 *354*(6315), 1027–1031. doi: 10.1126/science.aag0482
- 875 Brace, W. F., & Kohlstedt, D. L. (1980, nov). Limits on lithospheric stress imposed  
 876 by laboratory experiments. *Journal of Geophysical Research: Solid Earth*,  
 877 *85*(B11), 6248–6252. doi: 10.1029/jb085ib11p06248
- 878 Breuer, A., Heinecke, A., & Bader, M. (2016, jul). Petascale Local Time Step-  
 879 ping for the ADER-DG Finite Element Method. In *Proceedings - 2016*  
 880 *IEEE 30th International Parallel and Distributed Processing Symposium, IPDPS*  
 881 *2016* (pp. 854–863). Institute of Electrical and Electronics Engineers Inc.  
 882 doi: 10.1109/IPDPS.2016.109
- 883 Breuer, A., Heinecke, A., Rettenberger, S., Bader, M., Gabriel, A. A., & Pelties, C.  
 884 (2014). Sustained petascale performance of seismic simulations with SeisSol on  
 885 SuperMUC. In Kunkel J.M., Ludwig T., & Meuer H.W. (Eds.), *Lecture notes*  
 886 *in computer science (including subseries lecture notes in artificial intelligence*  
 887 *and lecture notes in bioinformatics)* (Vol. 8488 LNCS, pp. 1–18). Springer,  
 888 Cham. doi: 10.1007/978-3-319-07518-1\_1
- 889 Brodsky, E. E., Mori, J. J., Anderson, L., Chester, F. M., Conin, M., Dunham,  
 890 E. M., ... Yang, T. (2020). The State of Stress on the Fault Before, Dur-  
 891 ing, and After a Major Earthquake. *Annual Review of Earth and Planetary*  
 892 *Sciences*, *48*(1), 1–26. doi: 10.1146/annurev-earth-053018-060507
- 893 Brodsky, E. E., Saffer, D., Fulton, P., Chester, F., Conin, M., Huffman, K., ... Wu,  
 894 H.-Y. (2017, aug). The postearthquake stress state on the Tohoku megath-  
 895 rust as constrained by reanalysis of the JFAST breakout data. *Geophysical*  
 896 *Research Letters*, *44*(16), 8294–8302. doi: 10.1002/2017GL074027
- 897 Bürgmann, R. (2018, aug). The geophysics, geology and mechanics of slow fault slip.  
 898 *Earth and Planetary Science Letters*, *495*, 112–134. doi: 10.1016/j.epsl.2018.04  
 899 .062
- 900 Calahorrano, A., Sallarès, V., Collot, J.-Y., Sage, F., & Ranero, C. R. (2008).  
 901 Nonlinear variations of the physical properties along the southern Ecuador  
 902 subduction channel: Results from depth-migrated seismic data. *Earth and*  
 903 *Planetary Science Letters*, *267*(3), 453–467. doi: https://doi.org/10.1016/  
 904 j.epsl.2007.11.061
- 905 Chauhan, A. P. S., Singh, S. C., Hananto, N. D., Carton, H., Klingelhoefer, F.,  
 906 Dessa, J.-X., ... Graindorge, D. (2009, dec). Seismic imaging of forearc  
 907 backthrusts at northern Sumatra subduction zone. *Geophysical Journal Inter-*  
 908 *national*, *179*(3), 1772–1780. doi: 10.1111/j.1365-246X.2009.04378.x
- 909 Choy, G. L., & Boatwright, J. L. (1995). Global patterns of radiated seismic energy  
 910 and apparent stress. *Journal of Geophysical Research: Solid Earth*, *100*(B9),  
 911 18205–18228. doi: https://doi.org/10.1029/95JB01969
- 912 Cruz-Atienza, V. M., Villafuerte, C., & Bhat, H. S. (2018, dec). Rapid tremor mi-  
 913 gration and pore-pressure waves in subduction zones. *Nature Communications*,  
 914 *9*(1), 1–13. doi: 10.1038/s41467-018-05150-3
- 915 Day, S. M., Dalguer, L. A., Lapusta, N., & Liu, Y. (2005, dec). Comparison of  
 916 finite difference and boundary integral solutions to three-dimensional sponta-  
 917 neous rupture. *Journal of Geophysical Research: Solid Earth*, *110*(12), 1–23.  
 918 doi: 10.1029/2005JB003813
- 919 De La Puente, J., Ampuero, J. P., & Käser, M. (2009). Dynamic rupture model-  
 920 ing on unstructured meshes using a discontinuous Galerkin method. *Journal of*  
 921 *Geophysical Research: Solid Earth*, *114*(10). doi: 10.1029/2008JB006271
- 922 DeDontney, N., & Rice, J. R. (2011, dec). Tsunami Wave Analysis and Possibility of  
 923 Splay Fault Rupture During the 2004 Indian Ocean Earthquake. *Pure and Ap-*  
 924 *plied Geophysics*, *169*(10), 1707–1735. doi: 10.1007/s00024-011-0438-4
- 925 Denolle, M. A., & Shearer, P. M. (2016, sep). New perspectives on self-similarity  
 926 for shallow thrust earthquakes. *Journal of Geophysical Research: Solid Earth*,

- 927           121(9), 6533–6565. doi: 10.1002/2016JB013105
- 928 Dumbser, M., & Käser, M. (2006, oct). An arbitrary high-order discontinuous  
929 Galerkin method for elastic waves on unstructured meshes - II. The three-  
930 dimensional isotropic case. *Geophysical Journal International*, 167(1), 319–  
931 336. doi: 10.1111/j.1365-246X.2006.03120.x
- 932 Dunham, E. M., Belanger, D., Cong, L., & Kozdon, J. E. (2011, oct). Earthquake  
933 ruptures with strongly rate-weakening friction and off-fault plasticity, part 2:  
934 Nonplanar faults. *Bulletin of the Seismological Society of America*, 101(5),  
935 2308–2322. doi: 10.1785/0120100076
- 936 Dziewonski, A. M., Chou, T.-A., & Woodhouse, J. H. (1981, apr). Determination  
937 of earthquake source parameters from waveform data for studies of global and  
938 regional seismicity. *Journal of Geophysical Research: Solid Earth*, 86(B4),  
939 2825–2852. doi: 10.1029/JB086iB04p02825
- 940 Eberhart-Phillips, D., Han, D. H., & Zoback, M. D. (1989, feb). Empirical relation-  
941 ships among seismic velocity, effective pressure, porosity, and clay content in  
942 sandstone. *Geophysics*, 54(1), 82–89. doi: 10.1190/1.1442580
- 943 Ekström, G., Nettles, M., & Dziewoński, A. M. (2012, jun). The global CMT project  
944 2004-2010: Centroid-moment tensors for 13,017 earthquakes. *Physics of the  
945 Earth and Planetary Interiors*, 200-201, 1–9. doi: 10.1016/j.pepi.2012.04.002
- 946 Faulkner, D. R., Mitchell, T. M., Healy, D., & Heap, M. J. (2006, dec). Slip on  
947 ‘weak’ faults by the rotation of regional stress in the fracture damage zone.  
948 *Nature*, 444(7121), 922–925. doi: 10.1038/nature05353
- 949 Gabriel, A.-A., Ampuero, J.-P., Dalguer, L. A., & Mai, P. M. (2012). The tran-  
950 sition of dynamic rupture styles in elastic media under velocity-weakening  
951 friction. *Journal of Geophysical Research: Solid Earth*, 117(B9). doi: 10.1029/  
952 2012JB009468
- 953 Gabriel, A.-A., Ampuero, J.-P., Dalguer, L. A., & Mai, P. M. (2013, Au-  
954 gust). Source properties of dynamic rupture pulses with off-fault plas-  
955 ticity. *Journal of Geophysical Research: Solid Earth*, 118(8), 4117–4126.  
956 doi: 10.1002/jgrb.50213
- 957 Gabriel, A.-A., Vyas, J. C., Ulrich, T., Ampuero, J., & Mai, P. M. (2020). 3D dy-  
958 namic rupture modeling with thermal pressurization. In *Poster #158 at 2020  
959 seec annual meeting* (p. 08).
- 960 Gao, X., & Wang, K. (2014). Strength of stick-slip and creeping subduction megath-  
961 rustrs from heat flow observations. *Science*, 345(6200), 1038–1041. doi: 10  
962 .1126/science.1255487
- 963 Gao, X., & Wang, K. (2017). Rheological separation of the megathrust seismogenic  
964 zone and episodic tremor and slip. *Nature*, 543(7645), 416–419. doi: 10.1038/  
965 nature21389
- 966 Garagash, D. I. (2012, apr). Seismic and aseismic slip pulses driven by thermal pres-  
967 surization of pore fluid. *Journal of Geophysical Research: Solid Earth*, 117(4),  
968 n/a–n/a. doi: 10.1029/2011JB008889
- 969 Hardebeck, J. L. (2012, nov). Coseismic and postseismic stress rotations due to  
970 great subduction zone earthquakes. *Geophysical Research Letters*, 39(21), n/a–  
971 n/a. doi: 10.1029/2012GL053438
- 972 Hardebeck, J. L. (2015). Stress orientations in subduction zones and the strength of  
973 subduction megathrust faults. *Science*, 349(6253), 1213–1216. doi: 10.1126/  
974 science.aac5625
- 975 Hardebeck, J. L., & Hauksson, E. (2001). Crustal stressfield in southern Califor-  
976 nia and its implications for fault mechanics. *Journal of Geophysical Research*,  
977 106(B10), 21859–21882.
- 978 Harris, R. A., Barall, M., Aagaard, B., Ma, S., Roten, D., Olsen, K., . . . Dalguer,  
979 L. (2018, may). A Suite of Exercises for Verifying Dynamic Earth-  
980 quake Rupture Codes. *Seismological Research Letters*, 89(3), 1146–1162.  
981 doi: 10.1785/0220170222

- 982 Harris, R. A., Barall, M., Archuleta, R., Dunham, E., Aagaard, B., Ampuero, J. P.,  
 983 ... Templeton, E. (2009, jan). The SCEC/USGS dynamic earthquake rupture  
 984 code verification exercise. *Seismological Research Letters*, 80(1), 119–126.  
 985 doi: 10.1785/gssrl.80.1.119
- 986 Harris, R. A., & Day, S. M. (1997). Effects of a low-velocity zone on a dynamic rup-  
 987 ture. *Bulletin of the Seismological Society of America*, 87(5), 1267–1280.
- 988 Hayes, G. P., Wald, D. J., & Johnson, R. L. (2012, jan). Slab1.0: A three-  
 989 dimensional model of global subduction zone geometries. *Journal of Geo-  
 990 physical Research*, 117(B1), B01302. doi: 10.1029/2011JB008524
- 991 Heinecke, A., Breuer, A., Rettenberger, S., Bader, M., Gabriel, A. A., Pelties, C., ...  
 992 Dubey, P. (2014). Petascale High Order Dynamic Rupture Earthquake Simu-  
 993 lations on Heterogeneous Supercomputers. In *International conference for high  
 994 performance computing, networking, storage and analysis, sc* (Vol. 2015-Janua,  
 995 pp. 3–14). doi: 10.1109/SC.2014.6
- 996 Heise, W., Caldwell, T. G., Bannister, S., Bertrand, E. A., Ogawa, Y., Bennie, S. L.,  
 997 & Ichihara, H. (2017). Mapping subduction interface coupling using magne-  
 998 totellurics: Hikurangi margin, New Zealand. *Geophysical Research Letters*,  
 999 44(18), 9261–9266. doi: 10.1002/2017GL074641
- 1000 Heise, W., Caldwell, T. G., Bertrand, E. A., Hill, G. J., Bennie, S. L., & Ogawa,  
 1001 Y. (2013, oct). Changes in electrical resistivity track changes in tec-  
 1002 tonic plate coupling. *Geophysical Research Letters*, 40(19), 5029–5033.  
 1003 doi: 10.1002/grl.50959
- 1004 Houston, H. (2015). Low friction and fault weakening revealed by rising sensitivity  
 1005 of tremor to tidal stress. *Nature Geoscience*, 8(5), 409–415. doi: 10.1038/  
 1006 ngeo2419
- 1007 Huang, Y., Ampuero, J.-P., & Helmberger, D. V. (2014). Earthquake ruptures  
 1008 modulated by waves in damaged fault zones. *Journal of Geophysical Research:  
 1009 Solid Earth*, 119(4), 3133–3154. doi: https://doi.org/10.1002/2013JB010724
- 1010 Huang, Y., Ampuero, J.-P., & Helmberger, D. V. (2016). The potential for super-  
 1011 shear earthquakes in damaged fault zones—theory and observations. *Earth and  
 1012 Planetary Science Letters*, 433, 109–115.
- 1013 Hubbert, M. K., & Rubey, W. W. (1959, feb). Role of fluid pressure in me-  
 1014 chanics of overthrust faulting I. Mechanics of fluid-filled porous solids and  
 1015 its application to overthrust faulting. *GSA Bulletin*, 70(2), 115–166.  
 1016 doi: 10.1130/0016-7606(1959)70[115:ROFPIM]2.0.CO;2
- 1017 Hüpers, A., Torres, M. E., Owari, S., McNeill, L. C., Dugan, B., Henstock, T. J., ...  
 1018 Zhao, X. (2017, may). Release of mineral-bound water prior to subduction  
 1019 tied to shallow seismogenic slip off Sumatra. *Science*, 356(6340), 841–844.  
 1020 doi: 10.1126/science.aal3429
- 1021 Husen, S., & Kissling, E. (2002). Postseismic fluid flow after the large subduction  
 1022 earthquake of Antofagasta, Chile. *Geology*, 29(9), 847–850. doi: 10.1130/0091-  
 1023 -7613(2001)029(0847:PFFATL)2.0.CO;2
- 1024 Kaneko, Y., Lapusta, N., & Ampuero, J.-P. (2008). Spectral element modeling of  
 1025 spontaneous earthquake rupture on rate and state faults: Effect of velocity-  
 1026 strengthening friction at shallow depths. *Journal of Geophysical Research:  
 1027 Solid Earth*, 113(B9). doi: https://doi.org/10.1029/2007JB005553
- 1028 Karagianni, I., Papazachos, C. B., Scordilis, E. M., & Karakaisis, G. F. (2015).  
 1029 Reviewing the active stress field in Central Asia by using a modified stress  
 1030 tensor approach. *Journal of Seismology*, 19(2), 541–565. doi: 10.1007/  
 1031 s10950-015-9481-4
- 1032 Kozdon, J. E., & Dunham, E. M. (2013, may). Rupture to the Trench: Dynamic  
 1033 rupture simulations of the 11 march 2011 Tohoku earthquake. *Bulletin of  
 1034 the Seismological Society of America*, 103(2 B), 1275–1289. doi: 10.1785/  
 1035 0120120136
- 1036 Krenz, L., Uphoff, C., Ulrich, T., Gabriel, A.-A., Abrahams, L. S., Dunham, E. M.,

- 1037 & Bader, M. (2021, July). 3D Acoustic-Elastic Coupling with Grav-  
 1038 ity: The Dynamics of the 2018 Palu, Sulawesi Earthquake and Tsunami.  
 1039 *arXiv:2107.06640 [physics]*. (arXiv: 2107.06640)
- 1040 Lamb, S. (2006). Shear stresses on megathrusts: Implications for mountain building  
 1041 behind subduction zones. *Journal of Geophysical Research*, *111*(B7). doi: 10  
 1042 .1029/2005jb003916
- 1043 Laske, G., Masters, G., Ma, Z., & Pasyanos, M. (2013). Update on CRUST1.0—A  
 1044 1-degree global model of Earth’s crust. In *Egu general assembly 2013* (Vol. 15,  
 1045 p. 2658).
- 1046 Lay, T., Kanamori, H., Ammon, C. J., Koper, K. D., Hutko, A. R., Ye, L., ... Rush-  
 1047 ing, T. M. (2012, apr). Depth-varying rupture properties of subduction zone  
 1048 megathrust faults. *Journal of Geophysical Research: Solid Earth*, *117*(4), 4311.  
 1049 doi: 10.1029/2011JB009133
- 1050 Liu, Y., & Rice, J. R. (2005, aug). Aseismic slip transients emerge sponta-  
 1051 neously in three-dimensional rate and state modeling of subduction earth-  
 1052 quake sequences. *Journal of Geophysical Research: Solid Earth*, *110*(8), 1–14.  
 1053 doi: 10.1029/2004JB003424
- 1054 Liu, Y., & Rice, J. R. (2007, sep). Spontaneous and triggered aseismic deformation  
 1055 transients in a subduction fault model. *Journal of Geophysical Research: Solid  
 1056 Earth*, *112*(9), B09404. doi: 10.1029/2007JB004930
- 1057 Lotto, G. C., Jeppson, T. N., & Dunham, E. M. (2019, sep). Fully Coupled Simu-  
 1058 lations of Megathrust Earthquakes and Tsunamis in the Japan Trench, Nankai  
 1059 Trough, and Cascadia Subduction Zone. *Pure and Applied Geophysics*, *176*(9),  
 1060 4009–4041. doi: 10.1007/s00024-018-1990-y
- 1061 Ma, S. (2012, jun). A self-consistent mechanism for slow dynamic deformation and  
 1062 tsunami generation for earthquakes in the shallow subduction zone. *Geophysi-  
 1063 cal Research Letters*, *39*(11), n/a–n/a. doi: 10.1029/2012GL051854
- 1064 Ma, S., & Nie, S. (2019). Dynamic Wedge Failure and Along-Arc Variations of  
 1065 Tsunamigenesis in the Japan Trench Margin. *Geophysical Research Letters*,  
 1066 *46*(15), 8782–8790. doi: 10.1029/2019GL083148
- 1067 Madden, E. H., Bader, M., Behrens, J., Van Dinther, Y., Gabriel, A. A.,  
 1068 Rannabauer, L., ... Van Zelst, I. (2021, nov). Linked 3-D modelling of  
 1069 megathrust earthquake-tsunami events: From subduction to tsunami run  
 1070 up. *Geophysical Journal International*, *224*(1), 487–516. doi: 10.1093/gji/  
 1071 ggaa484
- 1072 Madden, E. H., Maerten, F., & Pollard, D. D. (2013). Mechanics of nonplanar faults  
 1073 at extensional steps with application to the 1992 M 7.3 Landers, California,  
 1074 earthquake. *Journal of Geophysical Research: Solid Earth*, *118*(6), 3249–3263.  
 1075 doi: 10.1002/jgrb.50237
- 1076 Madden, E. H., & Pollard, D. D. (2012). Integration of surface slip and aftershocks  
 1077 to constrain the 3D structure of faults involved in the M 7.3 landers earth-  
 1078 quake, Southern California. *Bulletin of the Seismological Society of America*,  
 1079 *102*(1), 321–342.
- 1080 Noda, H. (2008, sep). Frictional constitutive law at intermediate slip rates account-  
 1081 ing for flash heating and thermally activated slip process. *Journal of Geophysi-  
 1082 cal Research: Solid Earth*, *113*(9), B09302. doi: 10.1029/2007JB005406
- 1083 Noda, H., Dunham, E. M., & Rice, J. R. (2009, jul). Earthquake ruptures with  
 1084 thermal weakening and the operation of major faults at low overall stress  
 1085 levels. *Journal of Geophysical Research: Solid Earth*, *114*(7), B07302.  
 1086 doi: 10.1029/2008JB006143
- 1087 Oeser, J., Bunge, H. P., & Mohr, M. (2006). Cluster design in the earth sciences  
 1088 tethys. In *Lecture notes in computer science (including subseries lecture notes  
 1089 in artificial intelligence and lecture notes in bioinformatics)* (Vol. 4208 LNCS,  
 1090 pp. 31–40). Springer Verlag. doi: 10.1007/11847366\_4
- 1091 Oral, E., Weng, H., & Ampuero, J. P. (2020). Does a damaged-fault zone mit-

- 1092           igate the near-field impact of supershear earthquakes? application to the  
1093           2018 7.5 palu, indonesia, earthquake. *Geophysical Research Letters*, 47(1),  
1094           e2019GL085649. doi: <https://doi.org/10.1029/2019GL085649>
- 1095   Pelties, C., De La Puente, J., Ampuero, J. P., Brietzke, G. B., & Käser, M.   (2012,  
1096   feb).   Three-dimensional dynamic rupture simulation with a high-order dis-  
1097   continuous Galerkin method on unstructured tetrahedral meshes. *Journal*  
1098   *of Geophysical Research: Solid Earth*, 117(2), n/a–n/a.           doi: 10.1029/  
1099   2011JB008857
- 1100   Pelties, C., Gabriel, A. A., & Ampuero, J. P.   (2014).   Verification of an ADER-DG  
1101   method for complex dynamic rupture problems. *Geoscientific Model Develop-*  
1102   *ment*, 7(3), 847–866. doi: 10.5194/gmd-7-847-2014
- 1103   Pérez-Campos, X., & Beroza, G. C.   (2001).   An apparent mechanism dependence  
1104   of radiated seismic energy. *Journal of Geophysical Research: Solid Earth*,  
1105   106(B6), 11127–11136.   doi: <https://doi.org/10.1029/2000JB900455>
- 1106   Perez-Silva, A., Li, D., Gabriel, A.-A., & Kaneko, Y.   (2021). *3D modeling of long-*  
1107   *term slow slip events along the flat slab segment in the Guerrero Seismic Gap,*  
1108   *Mexico.*
- 1109   Perry, S. M., Lambert, V., & Lapusta, N.   (2020, mar).   Nearly Magnitude-  
1110   Invariant Stress Drops in Simulated Crack-Like Earthquake Sequences  
1111   on Rate-and-State Faults with Thermal Pressurization of Pore Fluids.  
1112   *Journal of Geophysical Research: Solid Earth*, 125(3), e2019JB018597.  
1113   doi: 10.1029/2019JB018597
- 1114   Petrini, C., Gerya, T., Yarushina, V., van Dinther, Y., Connolly, J., & Madonna, C.  
1115   (2020, sep).   Seismo-hydro-mechanical modelling of the seismic cycle: Method-  
1116   ology and implications for subduction zone seismicity. *Tectonophysics*, 791,  
1117   228504. doi: 10.1016/j.tecto.2020.228504
- 1118   Ramos, M. D., & Huang, Y.   (2019, feb).   How the Transition Region Along the  
1119   Cascadia Megathrust Influences Coseismic Behavior: Insights From 2-D Dy-  
1120   namic Rupture Simulations. *Geophysical Research Letters*, 46(4), 1973–1983.  
1121   doi: 10.1029/2018GL080812
- 1122   Ramos, M. D., Huang, Y., Ulrich, T., Li, D., Gabriel, A.-A., & Thomas, A. M.  
1123   (2021, July).   Assessing Margin-Wide Rupture Behaviors along the Cascadia  
1124   Megathrust with 3-D Dynamic Rupture Simulations. *Journal of Geophysical*  
1125   *Research: Solid Earth*, e2021JB022005.   (Publisher: John Wiley & Sons, Ltd)  
1126   doi: 10.1029/2021JB022005
- 1127   Rettenberger, S., Meister, O., Bader, M., & Gabriel, A.-A.   (2016).   ASAGI: A  
1128   Parallel Server for Adaptive Geoinformation.   In *Proceedings of the exascale*  
1129   *applications and software conference 2016* (pp. 2:1—2:9).   New York, NY,  
1130   USA: ACM.   doi: 10.1145/2938615.2938618
- 1131   Rice, J. R.   (1992).   Fault stress states , pore pressure distributions and the weaken-  
1132   ing of the San Andreas fault , in *Fault Mechanics and the Transport Properties*  
1133   *of Rocks : A Festschrift in Honor of W ...*   *Fault Mechanics and Transport*  
1134   *Properties of Rocks*(January 1992).
- 1135   Rice, J. R.   (2006, may).   Heating and weakening of faults during earthquake  
1136   slip. *Journal of Geophysical Research: Solid Earth*, 111(5).   doi: 10.1029/  
1137   2005JB004006
- 1138   Rowe, C. D., Meneghini, F., & Moore, J. C.   (2009, February).   Fluid-rich damage  
1139   zone of an ancient out-of-sequence thrust, Kodiak Islands, Alaska. *Tectonics*,  
1140   28(1). (Publisher: John Wiley & Sons, Ltd) doi: 10.1029/2007TC002126
- 1141   Saffer, D. M.   (2017).   Mapping fluids to subduction megathrust locking and slip  
1142   behavior. *Geophysical Research Letters*, 44(18), 9337–9340.   doi: 10.1002/  
1143   2017GL075381
- 1144   Saffer, D. M., & Tobin, H. J.   (2011, may).   Hydrogeology and mechanics of sub-  
1145   duction zone forearcs: Fluid flow and pore pressure. *Annual Review of Earth*  
1146   *and Planetary Sciences*, 39(1), 157–186.   doi: 10.1146/annurev-earth-040610

- 1147 -133408  
 1148 Schmitt, S. V., Segall, P., & Matsuzawa, T. (2011, jun). Shear heating-induced thermal  
 1149 pressurization during earthquake nucleation. *Journal of Geophysical Re-*  
 1150 *search: Solid Earth*, *116*(6), B06308. doi: 10.1029/2010JB008035  
 1151 Segall, P., & Bradley, A. M. (2012, sep). Slow-slip evolves into megathrust earth-  
 1152 quakes in 2D numerical simulations. *Geophysical Research Letters*, *39*(17),  
 1153 18308. doi: 10.1029/2012GL052811  
 1154 Segall, P., & Rice, J. R. (1995). Dilatancy, compaction, and slip instability of a  
 1155 fluid-infiltrated fault. *Journal of Geophysical Research*, *100*(B11), 22155–  
 1156 22171. doi: 10.1029/95jb02403  
 1157 Seno, T. (2017, jan). Subducted sediment thickness and Mw 9 earthquakes. *Jour-*  
 1158 *nal of Geophysical Research: Solid Earth*, *122*(1), 470–491. doi: 10.1002/  
 1159 2016JB013048  
 1160 Shearer, P., & Bürgmann, R. (2010). Lessons learned from the 2004 sumatra-  
 1161 andaman megathrust rupture. *Annual Review of Earth and Planetary Sci-*  
 1162 *ences*, *38*, 103–131. doi: 10.1146/annurev-earth-040809-152537  
 1163 Shelly, D. R., Beroza, G. C., & Ide, S. (2007, mar). Non-volcanic tremor and low-  
 1164 frequency earthquake swarms. *Nature*, *446*(7133), 305–307. doi: 10.1038/  
 1165 nature05666  
 1166 Shelly, D. R., Beroza, G. C., Ide, S., & Nakamura, S. (2006, jul). Low-frequency  
 1167 earthquakes in Shikoku, Japan, and their relationship to episodic tremor and  
 1168 slip. *Nature*, *442*(7099), 188–191. doi: 10.1038/nature04931  
 1169 Sibson, R. H. (1992, sep). Implications of fault-valve behaviour for rupture nucle-  
 1170 ation and recurrence. *Tectonophysics*, *211*(1-4), 283–293. doi: 10.1016/0040-  
 1171 -1951(92)90065-E  
 1172 Sibson, R. H. (1994, jan). Crustal stress, faulting and fluid flow. *Geological Society*  
 1173 *Special Publication*, *78*(1), 69–84. doi: 10.1144/GSL.SP.1994.078.01.07  
 1174 Sibson, R. H., & Rowland, J. V. (2003). Stress, fluid pressure and structural per-  
 1175 meability in seismogenic crust, North Island, New Zealand. *Geophysical Jour-*  
 1176 *nal International*, *154*(2), 584–594. doi: 10.1046/j.1365-246X.2003.01965.x  
 1177 Sibuet, J., Rangin, C., Lepichon, X., Singh, S., Cattaneo, A., Graindorge, D., ...  
 1178 Maury, T. (2007, nov). 26th December 2004 great Sumatra–Andaman earth-  
 1179 quake: Co-seismic and post-seismic motions in northern Sumatra. *Earth and*  
 1180 *Planetary Science Letters*, *263*(1-2), 88–103. doi: 10.1016/j.epsl.2007.09.005  
 1181 Singh, S. C., Carton, H., Tapponnier, P., Hananto, N. D., Chauhan, A. P., Har-  
 1182 toyo, D., ... Martin, J. (2008). Seismic evidence for broken oceanic crust in  
 1183 the 2004 Sumatra earthquake epicentral region. *Nature Geoscience*, *1*(11),  
 1184 777–781. doi: 10.1038/ngeo336  
 1185 Strasser, F. O., Arango, M., & Bommer, J. J. (2010). Scaling of the source dimen-  
 1186 sions of interface and intraslab subduction-zone earthquakes with moment  
 1187 magnitude. *Seismological Research Letters*, *81*(6), 941–950.  
 1188 Suppe, J. (2014). Fluid overpressures and strength of the sedimentary upper crust.  
 1189 *Journal of Structural Geology*, *69*(PB), 481–492. doi: 10.1016/j.jsg.2014.07  
 1190 .009  
 1191 Tarling, M. S., Smith, S. A., & Scott, J. M. (2019). Fluid overpressure from chem-  
 1192 ical reactions in serpentinite within the source region of deep episodic tremor.  
 1193 *Nature Geoscience*, *12*(12), 1034–1042. doi: 10.1038/s41561-019-0470-z  
 1194 Tobin, H. J., & Saffer, D. M. (2009, August). Elevated fluid pressure and extreme  
 1195 mechanical weakness of a plate boundary thrust, Nankai Trough subduction  
 1196 zone. *Geology*, *37*(8), 679–682. doi: 10.1130/G25752A.1  
 1197 Tonegawa, T., Kimura, T., Shiraishi, K., Yabe, S., Fukao, Y., Araki, E., ... Kodaira,  
 1198 S. (2021). Weak faults at megathrust plate boundary respond to tidal stress.  
 1199 *Earth, Planets and Space*, *73*(1), 89. doi: 10.1186/s40623-021-01414-3  
 1200 Townend, J., & Zoback, M. D. (2000, May). How faulting keeps the crust strong.  
 1201 *Geology*, *28*(5), 399–402. (Publisher: GeoScienceWorld) doi: 10.1130/0091

- 1202 -7613(2000)28(399:HFKTCS)2.0.CO;2
- 1203 Townend, J., & Zoback, M. D. (2004). Regional tectonic stress near the San Andreas  
1204 fault in central and southern California. *Geophysical Research Letters*, *31*(15),  
1205 1–5. doi: 10.1029/2003GL018918
- 1206 Uchide, T., Shearer, P. M., & Imanishi, K. (2014, sep). Stress drop variations among  
1207 small earthquakes before the 2011 Tohoku-oki, Japan, earthquake and impli-  
1208 cations for the main shock. *Journal of Geophysical Research: Solid Earth*,  
1209 *119*(9), 7164–7174. doi: 10.1002/2014JB010943
- 1210 Ulrich, T., Gabriel, A. A., Ampuero, J. P., & Xu, W. (2019, dec). Dynamic viability  
1211 of the 2016 Mw 7.8 Kaikōura earthquake cascade on weak crustal faults. *Nature*  
1212 *Communications*, *10*(1), 1213. doi: 10.1038/s41467-019-09125-w
- 1213 Ulrich, T., Gabriel, A.-A., & Madden, E. H. (2022). Stress, rigidity and sediment  
1214 strength control megathrust earthquake and tsunami dynamics. *Nature Geo-*  
1215 *science*, *15*(1), 67–73. doi: 10.1038/s41561-021-00863-5
- 1216 Ulrich, T., Vater, S., Madden, E. H., Behrens, J., van Dinther, Y., van Zelst, I., ...  
1217 Gabriel, A. A. (2019). Coupled, Physics-Based Modeling Reveals Earthquake  
1218 Displacements are Critical to the 2018 Palu, Sulawesi Tsunami. *Pure and*  
1219 *Applied Geophysics*, *176*(10), 4069–4109. doi: 10.1007/s00024-019-02290-5
- 1220 Uphoff, C., Rettenberger, S., Bader, M., Madden, E., Ulrich, T., Wollherr, S., &  
1221 Gabriel, A.-A. (2017). Extreme scale multi-physics simulations of the tsunami-  
1222 genic 2004 sumatra megathrust earthquake. In *Proceedings of the international*  
1223 *conference for high performance computing, networking, storage and analysis,*  
1224 *sc 2017*. doi: 10.1145/3126908.3126948
- 1225 Waldhauser, F., Schaff, D. P., Diehl, T., & Engdahl, E. R. (2012, jan). Splay faults  
1226 imaged by fluid-driven aftershocks of the 2004 Mw 9.2 Sumatra-Andaman  
1227 earthquake. *Geology*, *40*(3), 243–246. doi: 10.1130/G32420.1
- 1228 Wang, K., Brown, L., Hu, Y., Yoshida, K., He, J., & Sun, T. (2019, jun). Sta-  
1229 ble Forearc Stressed by a Weak Megathrust: Mechanical and Geodynamic  
1230 Implications of Stress Changes Caused by the M = 9 Tohoku-Oki Earth-  
1231 quake. *Journal of Geophysical Research: Solid Earth*, *124*(6), 6179–6194.  
1232 doi: 10.1029/2018JB017043
- 1233 Wang, X., & Morgan, J. K. (2019). Controls on Fore-Arc Deformation and Stress  
1234 Switching After the Great 2011 Tohoku-Oki Earthquake From Discrete Nu-  
1235 merical Simulations. *Journal of Geophysical Research: Solid Earth*, *124*(8),  
1236 9265–9279. doi: 10.1029/2019JB017420
- 1237 Weng, H., & Ampuero, J.-P. (2019). The dynamics of elongated earthquake rup-  
1238 tures. *Journal of Geophysical Research: Solid Earth*, *124*(8), 8584–8610.  
1239 doi: <https://doi.org/10.1029/2019JB017684>
- 1240 Wibberley, C. A., & Shimamoto, T. (2005, aug). Earthquake slip weakening and  
1241 asperities explained by thermal pressurization. *Nature*, *436*(7051), 689–692.  
1242 doi: 10.1038/nature03901
- 1243 Wirp, S. A., Gabriel, A.-A., Madden, E. H., Schmeller, M., van Zelst, I., Krenz, L.,  
1244 ... Rannabauer, L. (2021). 3D linked subduction, dynamic rupture, tsunami  
1245 and inundation modeling: dynamic effects of supershear and tsunami earth-  
1246 quakes, hypocenter location and shallow fault slip. *Frontiers in Earth Science*,  
1247 *9*, 177. doi: 10.3389/FEART.2021.626844
- 1248 Wolf, S., Gabriel, A. A., & Bader, M. (2020, jun). Optimization and local time step-  
1249 ping of an ader-dg scheme for fully anisotropic wave propagation in complex  
1250 geometries. In *Lecture notes in computer science (including subseries lecture*  
1251 *notes in artificial intelligence and lecture notes in bioinformatics)* (Vol. 12139  
1252 LNCS, pp. 32–45). Springer. doi: 10.1007/978-3-030-50420-5\_3
- 1253 Wollherr, S., Gabriel, A., & Mai, P. M. (2019, jul). Landers 1992 “Reloaded”: In-  
1254 tegrative Dynamic Earthquake Rupture Modeling. *Journal of Geophysical Re-*  
1255 *search: Solid Earth*, *124*, 2018JB016355. doi: 10.1029/2018JB016355
- 1256 Wollherr, S., Gabriel, A. A., & Uphoff, C. (2018, sep). Off-fault plasticity in

- 1257 three-dimensional dynamic rupture simulations using a modal Discontinuu-  
1258 ous Galerkin method on unstructured meshes: Implementation, verification  
1259 and application. *Geophysical Journal International*, 214(3), 1556–1584.  
1260 doi: 10.1093/GJI/GGY213
- 1261 Yao, S., & Yang, H. (2020, jun). Rupture Dynamics of the 2012 Nicoya Mw 7.6  
1262 Earthquake: Evidence for Low Strength on the Megathrust. *Geophysical Re-*  
1263 *search Letters*, 47(13). doi: 10.1029/2020GL087508
- 1264 Zelst, I., Wollherr, S., Gabriel, A., Madden, E. H., & Dinther, Y. (2019, nov).  
1265 Modeling Megathrust Earthquakes Across Scales: One-way Coupling From  
1266 Geodynamics and Seismic Cycles to Dynamic Rupture. *Journal of Geophysical*  
1267 *Research: Solid Earth*, 124(11), 11414–11446. doi: 10.1029/2019JB017539
- 1268 Zelst, I. v., Rannabauer, L., Gabriel, A.-A., & Dinther, Y. v. (2020). Earthquake  
1269 rupture on multiple splay faults and its effect on tsunamis. *EarthArXiv*, 1–  
1270 20.
- 1271 Zhu, W., Allison, K. L., Dunham, E. M., & Yang, Y. (2020, dec). Fault valving and  
1272 pore pressure evolution in simulations of earthquake sequences and aseismic  
1273 slip. *Nature Communications*, 11(1), 1–11. doi: 10.1038/s41467-020-18598-z